Selecting and modelling remnant AGNs with limited spectral coverage

Benjamin Quici [®],[1][★] Ross J. Turner [®],[2][★] Nicholas Seymour [®],[1] Natasha Hurley-Walker,[1]
Stanislav S. Shabala [®][2,3] and C. H. Ishwara-Chandra[4]

[1]*International Centre for Radio Astronomy Research, Curtin University, Bentley, WA 6102, Australia*
[2]*School of Natural Sciences, University of Tasmania, Private Bag 37, Hobart 7001, Australia*
[3]*ARC Centre of Excellence for All-Sky Astrophysics in 3 Dimensions (ASTRO 3D)*
[4]*National Centre for Radio Astrophysics, TIFR, Post Bag No. 3, Ganeshkhind Post, 411007 Pune, India*

ABSTRACT

Quantifying the energetics and lifetimes of remnant radio-loud active galactic nuclei (AGNs) is much more challenging than for active sources due to the added complexity of accurately determining the time since the central black hole switched off. Independent spectral modelling of remnant lobes enables the derivation of the remnant ratio, R_{rem} (i.e. 'off-time/source age'); however, the requirement of high-frequency ($\gtrsim 5\,\mathrm{GHz}$) coverage makes the application of this technique over large-area radio surveys difficult. In this work, we propose a new method, which relies on the observed brightness of backflow of Fanaroff–Riley type II lobes, combined with the *Radio AGN in Semi-Analytic Environments* (RAiSE) code, to measure the duration of the remnant phase. Sensitive radio observations of the remnant radio galaxy J2253-34 are obtained to provide a robust comparison of this technique with the canonical spectral analysis and modelling methods. We find that the remnant lifetimes modelled by each method are consistent; spectral modelling yields $R_{rem} = 0.23 \pm 0.02$, compared to $R_{rem} = 0.26 \pm 0.02$ from our new method. We examine the viability of applying our proposed technique to low-frequency radio surveys using mock radio source populations, and examine whether the technique is sensitive to any intrinsic properties of radio AGNs. Our results show that the technique can be used to robustly classify active and remnant populations, with the most confident predictions for the remnant ratio, and thus off-time, in the longest lived radio sources ($>50\,\mathrm{Myr}$) and those at higher redshifts ($z > 0.1$).

Key words: galaxies: active – galaxies: jets – radio continuum: galaxies.

1 INTRODUCTION

The supermassive black holes (SMBHs) residing at the heart of most galaxies (Magorrian et al. 1998; Häring & Rix 2004; Gültekin et al. 2009) play a profound role in the evolution of their host galaxies and large-scale (intergalactic) environments. Accretion on to the SMBH powers an active galactic nucleus (AGN), which, when radio-loud, drives a pair of jets comprising relativistic plasma. The jets inflate synchrotron-emitting lobes in the surrounding atmosphere, which act to heat up and expel the surrounding intergalactic gas, and eventually halt accretion on to the SMBH (see e.g. reviews by McNamara & Nulsen 2007; Alexander & Hickox 2012; Fabian 2012). This *jet mode* of AGN feedback is needed to quench star formation in the most massive galaxies (Croton et al. 2006), and to suppress cooling flows in the cores of massive clusters (Fabian et al. 2003) at low redshifts ($z \lesssim 2$–3; Fabian 2012).

Prescriptions for these feedback mechanisms require more than just the energetics and lifetimes of the jetted outbursts (Binney, Alouani Bibi & Omma 2007); the manner by which the jet power couples with the surrounding gas is equally as important (Tadhunter 2008; Alexander & Hickox 2012). The lifetime of the active jet phase has a large influence on the mechanism coupling the jet power

to the environment, e.g. through shock-heating driven by the global expansion of the lobes (Worrall et al. 2012), versus the clearing of gas through the late buoyant rise of jet-inflated bubbles (Churazov et al. 2001). This active lifetime also strongly maps to the radio source linear size (Kaiser & Alexander 1997), which determines the cluster radius of interaction where the energy deposition takes place. The duration of a quiescent phase, in which there is either no or reduced jet activity, can additionally be constrained from the active lifetime when combined with measurements of the duty cycle. The duty cycle can be directly constrained for 'double–double radio galaxies' (Schoenmakers et al. 2000) and some remnant radio galaxies (Turner 2018), or estimated on a population level from the radio-loud fraction (e.g. Best et al. 2005; Shimwell et al. 2019). Feedback mechanisms can therefore be examined by considering the spatial and temporal scales over which the energy deposition takes place, i.e. does the cluster environment have sufficient time to reach its equilibrium state before jet activity resumes (e.g. Turner & Shabala 2015).

The feedback mechanisms that regulate the supply of the surrounding gas are thought to give rise to an intermittency in jet activity, and the observed 'remnant' and 'restarted' radio galaxy populations (see e.g. reviews by Kapinska et al. 2015; Morganti 2017); the latter representing those in which jet activity has renewed prior to the remnant lobes fading from view. Importantly, remnant radio galaxies offer valuable constraints on the active lifetimes of AGN jets, necessary towards our general understanding of AGN jet feedback.

★ E-mail: benjamin.quici@icrar.org (BQ); turner.rj@icloud.com (RJT)

Shabala et al. (2020) demonstrate that models describing the global distribution of jet lifetimes and duty-cycles can be inferred from the observed fractions of remnant and restarted radio sources (relative to active ones). A direct measurement of the active jet lifetime can be made by modelling the dynamical evolution of remnant lobes (Turner 2018); the same is not true of the age derived for active radio lobes, which corresponds only to the age of the source at the time of observation, rather than the total lifetime of the jet. For these reasons, methods to select and model remnant radio galaxy lobes need to be robust.

Methodologies for selecting remnant radio galaxies are explored by many authors, particularly since the advent of the Low-Frequency Array (LOFAR; van Haarlem et al. 2013). The overall consensus, as first proposed by Brienza et al. (2016), is that a combination of morphological- and spectral-based methods is needed to select a representative sample of remnant radio galaxies.

It is possible to select remnants based on an ultra-steep (e.g. $\alpha \geq 1.2$; Cordey 1987), or highly curved (e.g. $\Delta\alpha \geq 0.5$; Murgia et al. 2011) radio spectrum criterion. These methods rely on sufficient fading (ageing) at the highest observing frequency, and will therefore miss recently switched-off remnants in which the break frequency lies beyond this frequency; this is confirmed based on observed and mock radio source populations (see e.g. Brienza et al. 2017; Godfrey, Morganti & Brienza 2017; Mahatma et al. 2018; Shabala et al. 2020). The bias associated with these spectral-based methods can be mitigated through the inclusion of a morphological-based selection, where remnant lobes are selected based on diffuse, low surface-brightness, amorphous lobes (e.g. Blob 1; Brienza et al. 2016); however, such methods may be less effective for recently switched-off remnants (e.g. 3C 28; Harwood, Hardcastle & Croston 2015).

Upon cessation of the jets, a bright radio core is expected to disappear rapidly (< 0.1 Myr). The selection of remnant radio galaxies can therefore also be made based on the absence of compact radio emission from the core (e.g. Mahatma et al. 2018; Quici et al. 2021); however, we note the recent results of Jurlin et al. (2021) who demonstrate the coexistence of faint radio emission from the core together with ultra-steep remnant radio lobes for a handful of objects. Their results suggest radio emission from the core, alone, may not necessarily determine whether the radio galaxy is active, and that high-frequency ($\nu \gtrsim 5$ GHz) observations are needed to confirm whether radio galaxy lobes are truly remnant.

High-frequency radio observations are also critical to modelling the energetics of both active and remnant AGNs (Turner, Shabala & Krause 2018b). Ageing of the lobe plasma results in a spectral steepening due to the preferential radiating of high-energy electrons (Kardashev 1962; Pacholczyk 1970), and is characterized by an optically thin break frequency that can be related (given a lobe magnetic field strength) to the plasma spectral age. However, a major challenge in modelling the dynamical evolution of remnant AGNs comes from the unknown time since the jets switched off. Turner (2018) show that this problem can be resolved by modelling the fractional duration of the remnant phase, based on the observed steepening in the integrated lobe spectrum, reducing the required model complexity to that of active radio sources. However, this method requires a well-sampled radio spectrum, where high-frequency ($\nu \gtrsim 5$ GHz) observations are often needed to properly characterize the observed spectral curvature.

Sensitive, wide-area radio surveys conducted with telescopes such as LOFAR; the Karoo Array Telescope (MeerKAT; Jonas & MeerKAT Team 2016); the Australian Square Kilometre Array Pathfinder (ASKAP; Johnston et al. 2007); and eventually the Square Kilometre Array (SKA) are expected to offer an unprecedented view of the radio galaxy life cycle. In principle, such surveys enable the compilation of large samples of active, remnant, and restarted radio sources, which will offer invaluable constraints on mechanisms describing the jet-triggering and AGN feedback. However, it is unrealistic to expect matching, high-frequency ($\nu \gtrsim 5$ GHz) sky coverage which, at present, is needed to robustly confirm the status of remnant lobes (Jurlin et al. 2021), and tightly constrain their energetics (Turner 2018).

In this work, we therefore explore whether measurements of the off-times of remnant lobes can be made based on their surface brightness distributions. To do this, we collect new data, presented in Section 2, for the remnant radio galaxy J2253-34 (see Quici et al. 2021), which are needed to conduct various spectral and dynamical modelling of the source. In Section 3, we apply an established spectral ageing method to provide an independent measurement of the off-time in J2253-34. In Section 4, we develop a new dynamical model-based method that uses the observed lobe backflow to measure the off-times in remnant radio galaxies. Here, we apply our method to J2253-34, and validate the estimate of its off-time against that derived previously from its radio spectrum. In Section 5, we use mock radio source populations, simulated at 150 MHz and 1.4 GHz, to examine whether the off-times in a wide range of remnants can be constrained by this method. Final discussions and conclusions are summarized in Section 6.

The Λ cold dark matter concordance cosmology with $\Omega_M = 0.3$, $\Omega_\Lambda = 0.7$, and $H_0 = 70 \, \mathrm{km \, s^{-1} \, Mpc^{-1}}$ (Komatsu et al. 2011) is assumed throughout the paper.

2 DATA

In this section, we describe the observations taken as part of this work, or larger observing projects, for J2253-34, and the methods used to image these data. We use new data collected by the Australia Telescope Compact Array (ATCA; Frater, Brooks & Whiteoak 1992), MeerKAT, and the upgraded Giant Meterwave Radio Telescope (uGMRT), together with several ancillary data products. A multiwavelength view of J2253-34 using these new data can be seen in Fig. 1. All measurements of the integrated flux density are reported in Table A1.

2.1 ATCA data

Pointed observations of J2253-34 were awarded through a series of observing proposals (Table 1). Observations were conducted within the 4 cm band, which allows simultaneous observing over two 2 GHz-wide bands which were centred at 5.5 and 9 GHz. The collection and reduction of these data are presented below.

To produce images with high spatial-resolution and sensitivity to large-scale structure, coverage of the (u, v) plane was maximized by observing in various ATCA configurations (see Table 1). Baselines ranged between 31 and 5939 m, ensuring an appropriate sampling of the largest angular scale of J2253-34 ($\theta \sim 100$ arcsec). The combined integration time on the target was 39.5 h.

At the beginning of each observation, we observed PKS B1934-638 for 10 min to derive bandpass, gain, and flux calibration solutions. 12 min scans of J2253-34 were interleaved with 2-min scans of PKS B2255-282; a source used to calibrate the time-varying gains.

Data reduction was performed using the Multichannel Image Reconstruction, Image Analysis and Display (MIRIAD; Sault, Teuben & Wright 1995), and closely followed the method outlined by Huynh et al. (2015, 2020); we used the primary scan to solve for the shape of the bandpass, the secondary scan to calibrate for the time-varying
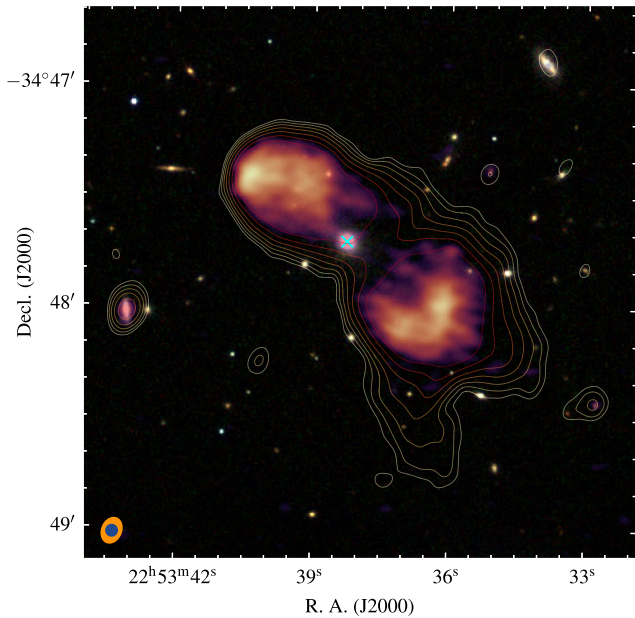
Figure 1. The remnant radio galaxy J2253-34 and its intergalactic environment. The background image is an RGB composite constructed from mid-infrared K_s (red), H (green), and J (blue) bands, respectively (see e.g. Quici et al. 2021). The host galaxy is indicated by a cyan-coloured 'x' marker. A 5.5 GHz view of J2253-34 with 4 arcsec resolution is superimposed on to the background. The coloured contours show the 1.42 GHz radio emission ('sub-band 3' in Section 2.2), with levels increasing uniformly in log-space by 0.2 dex in the range $[3, 80] \times \sigma$. Ellipses in the lower left corner denote the shape of the restoring beam at 1.42 GHz (orange) and 5.5 GHz (blue).

gains and the polarization leakages, and then transferred the solutions to J2253-34 where the gain solutions were averaged over a 2-min interval (the length of each phase calibrator scan). Throughout all these steps, channels known to be contaminated by radio frequency interference (RFI) were automatically flagged.

Calibrated data sets associated with each unique observation, with equal weighting, into a single data set. To improve the imaging dynamic range, three rounds of phase-only self-calibration were conducted using a `Robust 0.0` Briggs weighting (Briggs 1995), corresponding to an image resolution of approximately 3 arcsec × 6 arcsec. For each round, gains were solved over 2, 1, and 0.5 min time intervals, respectively. We refer to these data below as the 'calibrated data set', and discuss the synthesis of our science-ready images in Sections 2.1.1 and 2.1.2. For these data, we assume a 3 per cent calibration uncertainty in the ATCA flux density scale (Reynolds 1994).

2.1.1 Low-resolution imaging

We first produced images with lower spatial resolution to improve constraints on the high-frequency, integrated, spectral energy distribution. This was done by splitting each 2-GHz band of the calibrated data set into four 512 MHz sub-bands. Each sub-band was imaged in MIRIAD using a `Robust 0.0` Briggs weighting, with an additional 30 arcsec Gaussian taper on the visibilities so as to reduce contribution and noise from the longer baselines. The data were CLEANed to an initial depth of 3σ, after which a deeper CLEAN to 1σ was performed around pixels already in the model. Images were corrected for attenuation of the primary beam.

To extract the photometry, we used POLYGON_FLUX,[1] which uses the shape of the restoring beam to evaluate a background-subtracted integrated flux density corresponding to a user-defined region (see e.g. Hurley-Walker et al. 2019). Measurement uncertainties were calculated by multiplying the root mean square (RMS) noise by the square-root number of beams corresponding to the region volume, which we added in quadrature with the absolute calibration uncertainty.

2.1.2 High-resolution imaging

We further produced images with high spatial resolution so we could map the radio spectrum across the lobes (in conjunction with our data at other frequencies). To maximize signal-to-noise, we imaged the entire 2 GHz bandwidth available in each wide-band. To produce these images, we used a `uniform` Briggs weighting and applied an 8 arcsec taper to the visibilities; although it was possible to improve the spatial resolution beyond $\theta_{FWHM} = 8$ arcsec, this corresponded to the best possible circular resolution that could be achieved across all radio images presented in this work. To demonstrate this in Fig. 1, we present a higher resolution view of J2253-34 at 5.5 GHz by instead applying a 4 arcsec taper to the visibilities. The data were CLEANed to an initial depth of 3σ, after which a deeper CLEAN to 1σ was performed around pixels already in the model. After correcting images for the frequency-dependent primary beam attenuation, they achieved an RMS sensitivity of 11 and 13 μJy beam^{-1} at 5.5 and 9 GHz, respectively. We refer to these images as 'high-resolution ATCA images'.

2.2 MeerKAT data

We obtained 3.5 h of time to observe J2253-34 on the MeerKAT radio telescope (PI: B. Quici, project code: MKT 20212). Observations took place in the 'L band' (0.89–1.71 GHz), thus offering sensitive, high spatial-resolution observations at an intermediate-frequency range. To collect the data, we used PKS 1934-638 to calibrate the bandpass, and PKS 2259-37 to calibrate the time-varying gains. The MeerKAT bandpass response is stable to within 3 per cent over 2–3 h. As such, the observations were conducted in two 'blocks' by visiting the bandpass calibrator twice; once at the beginning of the observation, and again 1.5 h later. Each bandpass calibrator scan lasted 10 min. Observations of J2253-34 were carried out by interleaving a 2 min gain calibrator scan with a 15.5 min target scan. In total, the target received 2.6 h of exposure time. Using the calibrated measurement set made available from the South African Radio Astronomy Observatory (SARAO) Web Archive,[2] we performed a single round of RFI flagging using AOFlagger (Offringa, van de Gronde & Roerdink 2012). We identified four frequency ranges as having RFI-clean, unflagged visibilities, and we refer to these as 'sub–bands' (see Table A1).

Imaging was conducted using WSClean (Offringa et al. 2014). Each sub-band was imaged independently by blindly CLEANing the data down to a depth of 3σ, followed by a deeper CLEAN down to a 1σ level around the model. Imaging of sub-bands 1–4 was performed using an image weighting of `robust -1.0`, `-0.6`, `0.0`, and `+0.25`, respectively. In this way, all but the lowest sub-band achieved an image resolution of $\theta_{FWHM} \lesssim 8$ arcsec. All imaging was performed using the `multiscale` option, which enables multiscale

---

[1] https://github.com/nhurleywalker/polygon-flux
[2] The SARAO Web Archive is found at https://archive.sarao.ac.za/

Table 1. Summary of the new ATCA observations in different configurations described in Section 2.1. In order, columns denote the principal investigator; the project code; the ATCA configuration; the date of observation, each conducted during the year 2021; the total integration time; the range of shortest to longest baseline lengths; and the largest recoverable scales at 5.5 and 9 GHz. We note that B_{max} quoted for all but the 6C configuration excludes baselines formed with the $\sim$6 km outrigger antenna (CA06), due to the gap in (u, v) coverage.

PI	Project code	Config.	Date mm-dd	t (h)	$B_{min} - B_{max}$ (m)	$\theta_{max, 5.5}$ (arcmin)	$\theta_{max, 9}$ (arcmin)
Benjamin Quici	C3335	H75	06-03	8	31–89	6.0	3.7
	C3335	H168	07-22	5.5	61–185	3.1	1.9
	C3402	750C	02-14	12	46–704	4.1	2.5
	C3402	1.5A	01-03	12	153–1469	2.4	1.5
	C3402	6C	11-(12, 15)	10	337–5939	1.2	0.7

deconvolution (Offringa & Smirnov 2017). Each sub-band was then corrected for the frequency-dependent primary beam attenuation. Finally, images associated with sub-bands 2–4 were convolved to a circular 8 arcsec resolution, in order to match the resolution in the high-resolution ATCA images. The image associated with sub-band 1 was excluded from this final step, as the restoring beam exceeded 8 arcsec. A 5 per cent calibration uncertainty is assumed throughout this work. Following the method as described in Section 2.1.1, the integrated flux density of J2253-34 (and associated measurement uncertainty) was measured from each sub-band using the same user-defined polygon.

2.3 uGMRT data

We finally used two low-frequency, high-resolution radio images, created using data collected with the uGMRT, which contained J2253-34 within their fields of view. Observations were conducted in band 3 (250–500 MHz; proposal code 37_057, PI: Ross Turner), and in band 4 (550–900 MHz; proposal code 35_022, PI: C. H. Ish-wara Chandra). The data were reduced using the CAPTURE Pipeline (Kale & Ishwara-Chandra 2021), which uses the Common Astronomy Software Applications (CASA; McMullin et al. 2007) package. After the initial gain calibration, the data were channel averaged to keep the bandwidth smearing negligible. Using a Briggs weighting of robust 0.0, the channel averaged source data were subjected to four rounds of phase-only self-calibration followed by four more rounds of amplitude and phase self-calibration. A final band-3 image, centred at 417 MHz, was produced using a robust 0.0 weighting, resulting in a native resolution of $\sim$8 arcsec $\times$ 5 arcsec. A final band-4 image, centred at 682 MHz, was produced using a robust 0.0 weighting, resulting in a native resolution of $\sim$5 arcsec $\times$ 3 arcsec. The resolution in each image was convolved to a circular beam of $\theta = 8$ arcsec, achieving a local RMS of 52 and 43 μJy beam^{-1} at 417 and 682 MHz, respectively.

2.4 Ancillary data

To fill out the sampled integrated radio spectrum of J2253-34, particularly at frequencies not covered by our new data, we take several measurements previously compiled by Quici et al. (2021). We take their integrated flux densities reported at 119 and 154 MHz, measured from the GaLactic and Extragalactic All-sky Murchison Widefield Array (GLEAM; Hurley-Walker et al. 2017) survey; 887 MHz, measured from the Evolutionary Map of the Universe (EMU; Norris 2011); 1.4 GHz, measured from the NRAO VLA Sky Survey (NVSS; Condon et al. 1998), and; 2 and 2.868 GHz, measured

using pointed observations collected in the *LS* band ($\lambda = 4$ cm) of ATCA (see Table A1).

3 SPECTRAL MODELLING OF REMNANT LOBES

Before we develop a new method to measure the off-time in remnant radio sources, we must ensure that our result can be verified against an established method. The off-time can be derived from the rapid steepening of their high-frequency spectrum due to the cessation of the jet activity and the subsequent lack of freshly shock-accelerated synchrotron-emitting electrons. In Sections 3.1–3.3, we outline the theory of several literature-established spectral ageing models, and discuss their applications to radio lobe spectra. In Section 3.4, these models are applied to a combination of low- and high-resolution radio observations, in order to tightly parametrize the spectral ageing observed for J2253-34. Further, in Section 3.2, we briefly describe a PYTHON package we developed as part of this work to model synchrotron spectra for a diverse range of applications in astrophysics.

3.1 Synchrotron emissivity

The total emissivity of a synchrotron-emitting plasma, $J(\nu)$, can be found by integrating the single-electron emissivity (e.g. $j(\nu)$; Longair 2011) over the distribution of electron energies, $N(E)$, and the probabilistic distributions of the magnetic field strength, p_B, and pitch angle, p_ξ (equation 4 of Hardcastle 2013)

$$J(\nu) = \int_0^\infty \int_0^\pi \int_0^\infty \frac{\sqrt{3}Be^2 \sin\xi}{8\pi^2\epsilon_0 cm_e} F(x)N(E)p_\xi p_B \, dE \, d\xi \, dB, \quad (1)$$

where B gives the magnetic field strength, ξ the pitch angle, c the speed of light, e the electron charge, ϵ_0 the permittivity of free space, and m_e the electron mass. Rybicki & Lightman (1979) define $F(x)$ as the shape of the single-electron radiation spectrum, where x represents a dimensionless parametrization of frequency, magnetic field strength, and electron energy, E, through

$$x = \frac{\nu}{\nu_b} = \frac{4\pi m_e^3 c^4 \nu}{3e E^2 B \sin\xi}, \quad (2)$$

where ν_b is the break frequency above which (i.e. at higher frequencies) the spectrum steepens due to energy losses associated with the plasma ageing. Importantly, for a given magnetic field strength, the break frequency is related to the plasma spectral age through

$$\tau = \frac{\upsilon B^{1/2}}{B^2 + B_{IC}^2} \left(\nu_b(1 + z)\right)^{-1/2}, \quad (3)$$

where $B_{IC} = 0.318(1 + z)^2$ nT gives the magnetic field equivalent of the cosmic microwave background (CMB) at redshift z, and υ is a constant of proportionality (see equation 4 of Turner et al. 2018b).

Parametrization of meaningful attributes, such as ν_b, demands appropriate treatment of $N(E)$, p_B, and p_ξ. Kardashev (1962) initially proposed a model with no pitch angle scattering, giving $p_\xi = 1$; however, a more realistic model assuming an isotropic distribution for the pitch angle was subsequently suggested by Jaffe & Perola (1973), giving $p_\xi = \frac{1}{2}\sin\xi$; we assume the latter probabilistic distribution for the pitch angle in this work. Meanwhile, it is common to assume a locally uniform magnetic field, such that $p_B = 1$; however, this assumption is likely not physical due to the turbulent mixing of lobe plasma. Tribble (1991) provides an alternative treatment for a turbulent (non-uniform) magnetic field, in which the field strength is drawn from a Maxwell–Boltzmann distribution; here, p_B is satisfied by

$$p_B = \sqrt{\frac{2}{\pi}} \frac{B^2 \exp\left(-B^2/2a^2\right)}{a^3}, \tag{4}$$

where $a = B_0/\sqrt{3}$ for mean magnetic field strength, B_0 (Hardcastle 2013). These assumptions can be paired together with an appropriate treatment of the electron energy distribution of the underlying plasma, $N(E)$ (described below), to create a range of spectral ageing models; these are referred to as either the 'standard' (uniform B) or 'Tribble' (Maxwell–Boltzmann distribution B) forms of each spectral ageing model.

3.1.1 Impulsive injection models

The radio spectrum arising from an impulsively injected electron population is modelled as an ensemble of equal-age electrons [t, $t + \mathrm{d}t$] injected at $t = 0$ (Kardashev 1962; Jaffe & Perola 1973). Electrons are injected with an initial power-law distribution of energies, e.g. $N(E) = N_0 E^{-s}$, where the power-law energy index, s, is related to the injection spectral index, α_{inj}, through $s = 2\alpha_{\mathrm{inj}} + 1$. Synchrotron and inverse-Compton (IC) radiative losses, the latter due to upscattering of CMB photons, occur as the electron packet ages; the resulting effect on the energy distribution is well understood (see e.g. Pacholczyk 1970; Longair 2011). In the case of a uniform magnetic field, we follow the method of Turner et al. (2018b) to remove the dependence on B by recasting $N(E)$ to

$$N(x) = x^{-1/2} \begin{cases} \left(x^{1/2} - \iota^{1/2}\right)^{s-2} & x > \iota \\ 0 & x < \iota \end{cases}, \tag{5}$$

where $\iota(\nu, \xi) = \nu/(\nu_b \sin\xi)$ assuming an isotropic distribution for the pitch angle, as proposed by Jaffe & Perola (1973). Here, the total synchrotron emissivity is thus evaluated as

$$\mathcal{J}(\nu) = J_0 \nu^{(1-s)/2} \int_0^{\pi/2} \sin^{(s+3)/2}\xi \int_0^\infty F(x)N(x)\,\mathrm{d}x\,\mathrm{d}\xi, \tag{6}$$

where J_0 acts as a frequency-independent constant. In this work, we refer to this impulsively injected spectral ageing model as the 'standard' Jaffe-Parola (or JP) model. Importantly, parametrizing the shape of this standard JP spectrum in this way only requires knowledge of the injection index and break frequency. By comparison, the shape of a 'Tribble' Jaffe-Parola (or TJP) model spectrum additionally requires knowledge of B.

Considering some small region across a radio galaxy lobe [e.g. bounded by the full width at half-maximum (FWHM) of a restoring beam], it is reasonable to suspect that the plasma contained here will have been injected at approximately the same age. This means that

the associated radio spectrum is likely that of the JP model; however, we note the results of Turner et al. (2018a), Mahatma et al. (2020), Yates-Jones, Shabala & Krause (2021), and Yates-Jones et al. (2022), who show that mixing of plasma ages may violate this assumption.

3.1.2 Continuous injection models

The above assumption of an impulsively injected packet of electrons breaks down when considering the integrated spectrum of a radio AGN, which comprises multiple, or on-going, such injections throughout the lifetime of the source. A continuous injection model describes a radio spectrum arising from a time-averaged population of continuously injected electron packets; that is, a mixed-age plasma population with ages ranging within $[0, \tau]$. In the simpler and more common case, the CI model assumes continuous injection via an active jet throughout the entire lifetime of the source (e.g. the 'CI-on' or CIJP[3] model). To model remnant AGNs, Komissarov & Gubanov (1994) present an extension to the CI model, known as the 'CI-off' or KGJP model, by instead assuming some fraction of the total source age, $R_{\mathrm{rem}} = t_{\mathrm{rem}}/\tau$, is spent in a remnant phase; we refer to R_{rem} as the remnant ratio, where the total source age, τ, is given by the sum of the active and remnant durations, $\tau = t_{\mathrm{on}} + t_{\mathrm{rem}}$. As with the JP model, the effect of ageing on the plasma energy distribution is well understood (see e.g. Longair 2011). In the case of a uniform magnetic field, the recast form of $N(E)$ is given by (equation 3 of Turner 2018)

$$\mathcal{N}(x) = x^{-1/2} \begin{cases} \left(x^{-1/2} - \zeta^{1/2}\right)^{s-1} - \left(x^{1/2} - \iota^{1/2}\right)^{s-1} & x > \iota \\ \left(x^{1/2} - \zeta^{1/2}\right)^{s-1} & \zeta \leq x \leq \iota \\ 0 & x < \zeta \end{cases}, \tag{7}$$

where $\zeta(\nu, \xi) = \iota(\nu, \xi)R_{\mathrm{rem}}^2$. The total synchrotron emissivity of a CI spectrum is thus derived by

$$\mathcal{J}(\nu) = J_0 \nu^{-s/2} \int_0^{\pi/2} \sin^{(s+4)/2}\xi \int_0^\infty F(x)N(x)\,\mathrm{d}x\,\mathrm{d}\xi, \tag{8}$$

In the limiting case where $R_{\mathrm{rem}} = 0$, the CI-off model reduces to the simpler CI-on form. For simplicity, we thus refer to the general form as the CI model. In this way, parametrizing the shape of a standard CI spectrum requires only the injection index, break frequency, and remnant ratio. As with the TJP model, the shape of a 'Tribble' Continuous Injection (or TCI) spectrum additionally requires knowledge of B.

Due to their assumption of a mixed-age plasma, the CI models are relevant for deriving the plasma spectral age from the integrated spectra of radio lobes (e.g. Parma et al. 2007; Murgia et al. 2011; Shulevski et al. 2012; Brienza et al. 2016; Turner 2018; Duchesne & Johnston-Hollitt 2019). However, it is worth mentioning that the CI model assumes no temporal evolution in the magnetic field, which we know not to be true for expanding lobes. Using synthetic radio source populations, for which all radiative losses and temporal evolution of the magnetic field were considered, Turner et al. (2018b) demonstrated that the radio emissivity reflects only the most recent ~ 10 per cent of the magnetic field history. Importantly, their results showed that the spectral age derived using the break frequency, parametrized by the CI model, together with the present-time magnetic field strength, was in agreement with the dynamical

---

[3]Here, the 'JP' reflects only the isotropic distribution for the pitch angle proposed by Jaffe & Perola (1973), not their assumption of an impulsively injected plasma.

age. As such, we can be confident that the quantities parametrized by the CI model are physically meaningful.

3.2 Spectral model fitting

We now discuss our approach taken to numerically implement the spectral ageing model described in the previous section, and to fit these spectra to observed data points. The code we developed to achieve this is expected to be highly valuable to the broader astrophysics community (e.g. synchrotron spectra from active galaxies, supernovae remnants, etc.), and so we have released it as the publicly available **synchro**tron spectral **fit**ter (SYNCHROFIT)[4] PYTHON library. Principally, SYNCHROFIT offers a suite of routines that: (1) implement the JP and CI spectral ageing models described in Sections 3.1.1 and 3.1.2, and (2) fit these models to real radio data.

For computational efficiency, the standard spectral ageing models are evaluated by numerically integrating over the electron energy and pitch angle, following the reduced dimensionality parametrization of $J(\nu)$, first presented by Nagai et al. (2006, JP), Turner et al. (2018b, CI-on), and Turner (2018, CI-off). The Tribble spectral ageing models are evaluated in a similar fashion, however involve an additional numerical integration over the magnetic field strength, and as such incur a considerable cost to the computation time. An injection index and break frequency are required to parametrize the shape of the JP spectrum, with an additional normalization to scale the fit appropriately. The shape of a CI spectrum is additionally parametrized by the remnant ratio, noting that $R_{\rm rem} = 0$ in the case of the CI-on model. Tribble forms of the spectral ageing models are parametrized similarly, however additionally require the redshift and magnetic field strength.

Fitting of these models is conducted using a grid-search informed by an adaptive maximum-likelihood algorithm. Discrete samples in s, $\log \nu_b$, and $R_{\rm rem}$ are created by uniformly sampling their allowed ranges, which are used to construct a three-dimensional parameter grid. A spectral model is evaluated for each unique parameter combination, where a corresponding normalization is optimized following $S_0 = \sum_{i=1}^{n}(S_{o_i} \times \sigma_i) - \sum_{i=1}^{n}(S_{p_i} \times \sigma_i)/\sum_{i=1}^{n}\sigma_i$, where n is the number of spectral measurements, S_{o_i} and S_{p_i} are the observed and predicted flux densities in logarithmic space, and σ_i is the measurement uncertainty for the ith datum. The quality of fit is evaluated using the lowest value of the Akaike information criterion (AIC; Akaike 1974) following $\mathrm{AIC} = 2k - 2\ln\mathcal{L}$, where k is the number of model parameters.[5] The likelihood function, $\mathcal{L}$, is defined through

$$\mathcal{L}(\mu, \sigma) = \prod_{i=1} \frac{1}{\sqrt{2\pi}\sigma_i} \exp\left(-\frac{(x_i - \mu_i)^2}{2\sigma_i^2}\right) \tag{9}$$

which, for each unique measurement, i, takes into consideration the observed value, x_i, measurement uncertainty, σ_i, and the corresponding predicted model value μ_i. Across all grid realizations, the set of parameters providing the optimal spectral fit are defined as those that minimize the AIC. The relative quality of each spectral fit is found using $p_i = e^{(\mathrm{AIC}_i - \mathrm{AIC}_{\rm best})/2}$, where p_i is the probability that the ith spectral model provides a better fit to the observations than the selected 'best' model. Provided the marginal probability density functions (PDFs) in each model parameter are pseudo-Gaussian, the

fitted uncertainty in each parameter is taken as the standard deviation, and the peak in the PDF as the approximate location of the global maximum. In order to increase the precision of the best estimate in each free parameter, a grid of points is then resampled around the global maximum; in this work, we repeat this over three iterations. We note that Gaussianity may not necessarily always hold for these PDFs, as this will depend upon the spectral fit, hence we make sure to inspect these throughout this work.

3.3 Effect of inhomogeneity in the local magnetic field

The standard form of the spectral ageing models have a considerable computational advantage over the (likely more physically accurate) Tribble forms in our implementation (due to the lower number of numerical integrations). We therefore investigate if the standard form can be used to reasonably approximate the Tribble form for either spectral ageing model, or for any range of magnetic field strengths.

Both the standard and Tribble forms of the spectral ageing models offer a physically meaningful parametrization of observed radio spectra. Due to the consideration of a variable magnetic field, the shape of the expected synchrotron spectrum differs with that in which the magnetic field is uniform. For example, Hardcastle (2013) shows a significant departure of the TJP model from the standard form, notably due to the sharper spectral turnover around the break frequency in the TJP spectrum. Turner et al. (2018b) explore the consequence of using the standard spectral ageing models to parametrize simulated Tribble spectra; their results demonstrate an overestimation of the break frequency, which appears to be more appreciable for the JP model as compared to the CI model.

The assumption of a locally uniform magnetic field will be at least somewhat violated in radio AGN lobes due to turbulent flow; the Maxwell–Boltzmann magnetic field distribution of the Tribble spectral ageing models may provide a more realistic description, however this in turn requires knowledge of B_0 which, unless independent X-ray data are available, would require dynamical modelling.

As such, we seek to explore the dependence of the shape of the Tribble spectral ageing models on B_0. We use SYNCHROFIT to simulate standard and Tribble forms of the JP and CI models, assuming $s = 2.2$, and $\nu_b = 2.1$ GHz. Tribble models are simulated for $B_0 = 0.1$, 1, and 10 nT, in order to cover a broad range of acceptable values. These are shown in Fig. 2.

As a consistency check with Hardcastle (2013), Harwood et al. (2013), and Turner et al. (2018b), we reassuringly find that integrating over a Maxwell–Boltzmann magnetic field modifies the shape of the predicted spectra to that in which the magnetic field is uniform. However, our results show that the shape of the predicted Tribble spectra are largely insensitive to values of the mean magnetic field strength. We find that electron packets with magnetic strengths in the exponential tail of the Maxwell–Boltzmann distribution (i.e. $B > \sqrt{3/2}\,B_0$) contribute the vast majority of the total synchrotron emission at all radio frequencies. Importantly, the mean magnetic field strength has no effect on the shape of this exponential portion of PDF, albeit modifies its normalization. As a result, the shape of the radio spectrum remains largely unaffected for moderate changes in the mean magnetic field. The implication here is it is possible to accurately parametrize the injection index, break frequency, and remnant fraction (in the case of the CI models), using the Tribble spectral ageing models without explicitly requiring knowledge of B_0; an informed guess of the mean magnetic field strength is sufficient (e.g. $B_0 \sim 0.1$–10 nT).

---

[4]https://github.com/synchrofit

[5]For the standard JP and CI-on models, $k = 3$. For the standard CI-off models, $k = 4$. In the case of the Tribble forms, k increases by 1 due to the magnetic field.
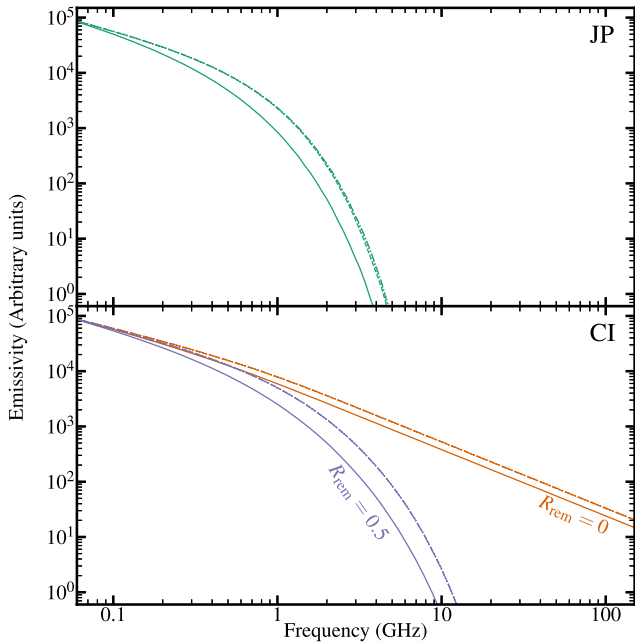
Figure 2. Comparison between standard (solid lines) and Tribble forms (broken lines) of the JP (top panel) and CI (bottom panel) spectra. SYNCHROFIT is used to simulate radio spectra for $s = 2.2$ and $\nu_b = 2.1$ GHz. Tribble models are shown for $B = 0.1$ nT (dot–dashed), $B = 1$ nT (dotted), and $B = 10$ nT (dashed). CI models are shown for $R_{rem} = 0$ (orange) and $R_{rem} = 0.5$ (purple). We note that the Tribble models almost exactly overlay each other and hence cannot be distinguished.

3.4 Modelling the radio spectrum of J2253-34

We are now equipped with the tools needed to derive a robust measurement of the off-time from our observations J2253-34. However, we choose not to directly fit the integrated spectrum with the CI-off model as the three parameters are somewhat correlated, and may be misfitted if our observations include moderate systematic uncertainties. Instead, we independently constrain the injection index by considering the spectra arising from narrow regions across the lobes; it is reasonable to assume these spectra can be described by the JP model (see Section 3.1.1). Assuming a constant injection index throughout the lifetime of the source, the JP models can be jointly fit to these spectra, resulting in a precise measurement of the injection index optimized across the lobes. The integrated spectrum can now be fitted using the CI model for a known injection index, reducing any potential systematic errors in estimates for the break frequency and remnant ratio; the latter mapping directly to the duration of the remnant phase for any given source age. This is described in detail below.

3.4.1 Modelling the injection index

To model the injection index, we use the 8 arcsec beam-matched radio maps described in Section 2. We use MIRIAD to create a 2D cut-out of J2253-34 from each image, and `regrid` the cut-outs to have a common pixel scale (d$\theta = 1$ arcsec) and projection (SIN). To efficiently sample the resolved radio spectrum, we extract the radio spectra arising from individual circular apertures arranged in a hexagonal configuration across the lobes. The FWHM of each aperture is set to $\theta_{FWHM} = 8$ arcsec to reflect the size of the restoring beam. The integrated flux density within each aperture is then calculated following $S_{int} = \sum_{i=1}^{n} S_{p,i} \times d\theta^2 / \Omega$, where n is the

number of pixels contained within each aperture, $S_{p,i}$ is the value of the ith pixel in Jy beam^{-1}, dθ is the pixel angular scale, and Ω is the beam solid angle defined as $\theta_{FWHM}^2 \times \pi/(4\ln 2)$. Given the spectra are extracted from exactly one resolution element, the measurement uncertainty is evaluated as the quadrature sum of the RMS noise in the observations and their absolute calibration uncertainty.

Following this method, the radio spectra are extracted from all regions across the lobes with 9 GHz radio emission above the 5σ noise level. This restriction is done so as to maximize the number of observing frequencies contributing to the radio spectrum. The spectra arising from each aperture are independently fit using the JP (and TJP) models; importantly both the break frequency and the injection index are free parameters in their corresponding aperture spectral fit. In light of the results in Section 3.3, we use equation (2) of Miley (1980) to calculate a crude approximation of the lobe equipartition magnetic field strength as $B_{eq} \approx 0.35$ nT. Considering also that radio galaxy lobes are typically sub-equipartition (see e.g. fig. 11 of Turner et al. 2018b), we fit the TJP model assuming $B_0 = 0.1, 0.35$, and 1 nT. Spectral models are evaluated by uniformly sampling the injection index within a range corresponding to [2.01, 2.99] and an initial grid spacing of $\Delta s = 0.05$. For each aperture spectral fit, a corresponding PDF is found by marginalizing across the fitted injection index. Each PDF is then multiplied together to determine which value for the injection index provides an optimal fit across all aperture spectra; this assumes no correlation between the spectra arising from adjacent apertures, and also assumes a constant injection index throughout the lifetime of the source. Following this method, we optimize an injection index by considering the spectra arising from both lobes, which we present in Fig. 3. Importantly, we found that the optimal injection index modelled using the standard JP model is found to be $s = 2.10 \pm 0.05$ (or $\alpha_{inj} = 0.550 \pm 0.025$). For the Tribble model, we found an optimal value of $s = 2.25 \pm 0.03$ (or $\alpha_{inj} = 0.625 \pm 0.015$).

3.4.2 Modelling the break frequency and remnant ratio

We compile an integrated radio spectrum for J2253-34 using the two decades of radio-frequency data described in Section 2. The raw spectrum is presented in Fig. 4, and demonstrates a clear spectral curvature owing to the losses associated with an inactive jet; this is evidenced by an ultra-steep high-frequency spectral index of $\alpha = 1.7$, computed between 4.5 and 9.5 GHz. With the injection index estimated in Section 3.4.1, we seek to model the break frequency and remnant ratio of J2253-34 by parametrizing the observed curvature using the CI spectral ageing models.

Similar to the resolved modelling to determine the injection index, we model the integrated spectrum using both the standard and Tribble forms of the CI model. For consistency, we use the injection indices estimated using the standard and Tribble JP models as inputs to the standard and Tribble CI models, respectively. Similarly, TCI models are evaluated for the same values of B_0 used in Section 3.4.1. To account for the small uncertainty in the injection index previously fitted by the JP models, we treat 's' as a free parameter in the CI models, but apply a tight Gaussian prior based on the fitted uncertainty. We find that fixing the injection index offers no appreciable difference to our results, unsurprising considering the uncertainties on the injection index are small. The CI model fitted to the integrated spectrum is shown in Fig. 4.

Results of the fitting are summarized as follows (see also Table 2). Modelling the integrated radio spectrum using the CI model gives a break frequency of $\nu_b = 1.78^{+0.17}_{-0.15}$ GHz, and a remnant ratio of
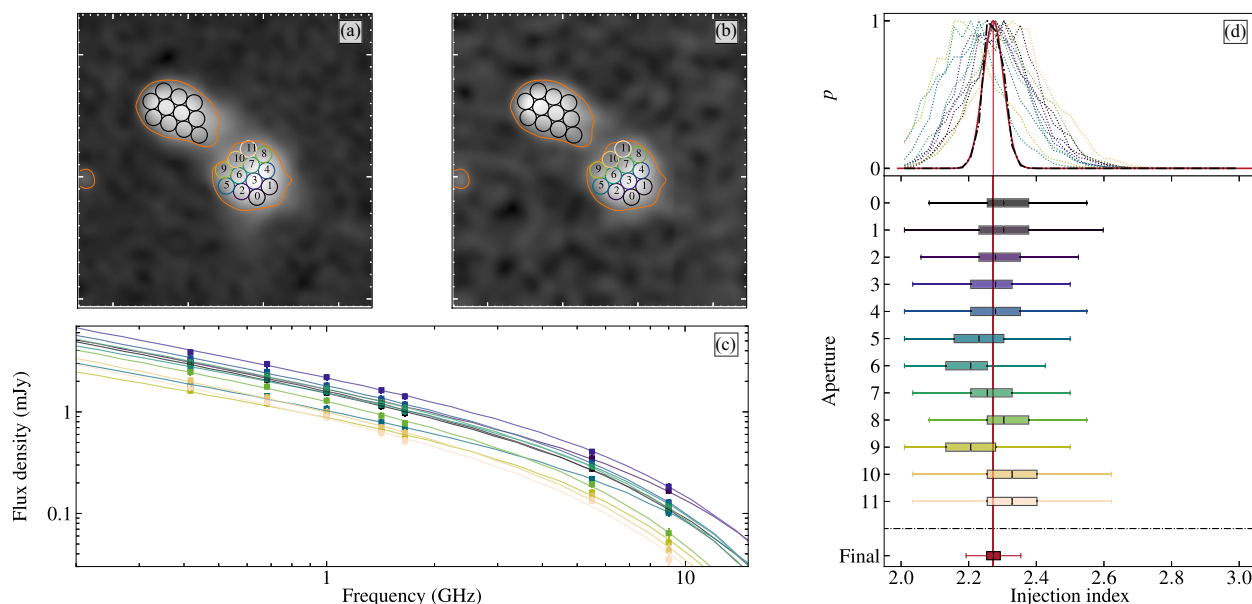
Figure 3. The injection index optimized for J2253-34. Panels (a) and (b) show the observed radio emission at 1.32 and 5.5 GHz, respectively; each image is presented on a square-root stretch, and is normalized between the minimum/maximum pixel values. A solid dark-orange contour denotes the 5σ brightness of the source at 9 GHz. Circular markers of an 8 arcsec aperture (the FWHM of the restoring beam) are used to represent independent regions from which a radio spectrum is extracted and used as a constraint on the injection index. Apertures overlaid on the south-western lobe are colour-coded and numbered based on aperture number, and are highlighted in panels (c) and (d); to avoid clutter in the figure we do not plot the spectral fits for apertures in the north-eastern lobe. Panel (c) demonstrates fits of the TJP model ($B_0 = 0.1$ nT) optimized to their associated spectrum. Panel (d) demonstrates the PDF associated with each spectral fit, marginalized with respect to the injection index; these are also represented by the box and whisker plots, where the box is constrained by the 25th–75th percentiles. A global optimization for the injection index is found by multiplying the PDFs associated with each lobe (dot–dashed black curve), which is then approximated by a 1D Gaussian (solid red curve) in order to characterize the peak probable value and uncertainty: $s = 2.25 \pm 0.03$ (or alternatively, the injection spectral index; $\alpha_{\rm inj} = 0.625 \pm 0.015$).
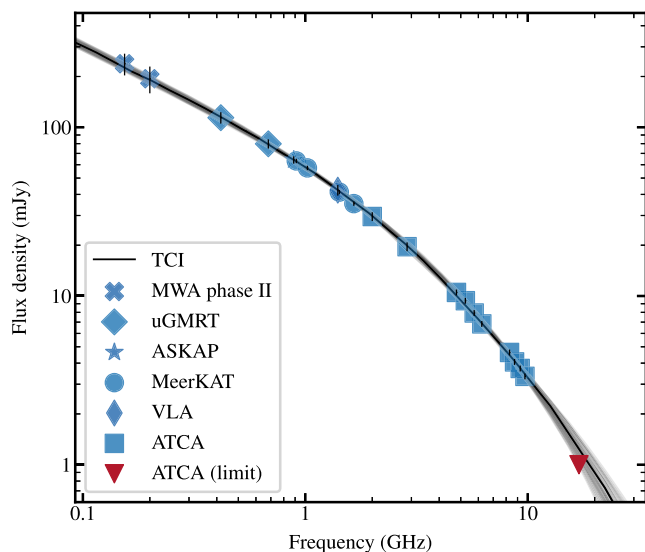

Figure 4. The spectral emissivity of J2253-34. Blue markers are used to display measurements of the integrated flux density. Error-bars represent 1σ measurement uncertainties. Overlaid is the fit of the TCI model, assuming $B_0 = 0.1$ nT and $s = 2.25 \pm 0.03$ (Section 3.4.1). The optimal fit of the TCI model (Section 3.4.2) is displayed using a solid black line. Also shown in light-grey are all plausible spectral fits within a 99.7 per cent (3σ) confidence interval. The spectral break frequency and remnant ratio are fitted as $\nu_{\rm b} = 1.26^{+0.06}_{-0.05}$ GHz, and $R_{\rm rem} = 0.23 \pm 0.02$, respectively.

Table 2. The spectral modelling attributes of J2253-34, described in Section 3.4. Using the 8 arcsec radio images, the radio spectra arising from small regions across the lobes are jointly fit by the JP models, in order to optimize the injection index. The broad-band integrated radio spectrum is then fit by the CI models, propagating the fitted injection index and uncertainties through a Gaussian prior, to estimate the break frequency and remnant ratio.

Model	Injection index	Break frequency	Remnant ratio
JP	2.10 ± 0.05	–	–
TJP	2.25 ± 0.03	–	–
CI	–	$1.78^{+0.17}_{-0.15}$ GHz	0.23 ± 0.02
TCI	–	$1.26^{+0.06}_{-0.05}$ GHz	0.23 ± 0.02

$R_{\rm rem} = 0.23 \pm 0.02$. Using instead the TCI model gives a marginally different break frequency of $\nu_{\rm b} = 1.26^{+0.06}_{-0.05}$ GHz, and remarkably, a remnant ratio of $R_{\rm rem} = 0.23 \pm 0.02$, consistent with the value constrained from the standard CI model.

Finally, it is important to mention that the precise measurements of the break frequency and remnant ratio of J2253-34 are only made possible by the independently fitted injection index. By inspecting the marginal distribution of the fitted break frequency and remnant ratio, we find that their PDFs are Gaussian-like, and importantly do not demonstrate any parameter degeneracy worth consideration. These results are in stark contrast to those found by blindly fitting each parameter of the CI models from the integrated radio lobe spectrum. Here, we find that a single precise measurement of the injection index cannot be found, e.g. for the standard CI model, the fitted injection index can plausibly be in the range $s \sim 2.1$–2.3. Consequently, this introduces major uncertainties on to the fitted break frequency and

remnant ratio, which become largely degenerate with one another, e.g. for the standard CI model, the break frequency demonstrates frequent local minima/maxima between $\nu_b \sim 2$ and $5\,\mathrm{GHz}$, and the PDF of the fitted remnant ratio is heavily asymmetric about its peak probable value of $R_{rem} \sim 0.38$. It is interesting that these results are found even for an integrated radio spectrum as well sampled as that of J2253-34, and thus reinforce the approach described in this section.

4 DYNAMICAL MODELLING OF REMNANT LOBES

In the following section, we present a new dynamical model-based method that measures the off-time in remnant lobes, and is capable of identifying candidate remnant radio galaxies from observations. In Section 4.1, we present the dynamical model that underpins this work. In Section 4.2, we justify why the backflow of lobe plasma holds valuable constraints on the off-time, and necessarily devise a tool to parametrize the surface brightness distribution of radio lobes. In Section 4.3, we then outline the constraints necessary to model the energetics of lobed radio-loud AGNs. Finally in Section 4.4, we implement our new method to constrain the energetics of J2253-34, which we then independently verify against the remnant ratio previously measured in Section 3.

4.1 Radio AGN in semi-analytic environments

Throughout this work, the *Radio AGN in Semi-analytic Environments* (RAiSE; Turner & Shabala 2015; Turner et al. 2018a; Turner & Shabala 2020) code is used to model the dynamics of Fanaroff & Riley type-II (FR-II; Fanaroff & Riley 1974) radio lobes. In this work, we employ RAiSE both as a tool to model the radio-loud AGN energetics, and to simulate mock radio source populations.

4.1.1 The RAiSE model

The RAiSE code consolidates models describing the expansion of lobed FR-II/I sources together with an observation-based treatment of the environments within which the jets expand; RAiSE has been tested to show consistency with hydrodynamical simulations, is able to reproduce the observed relationship between radio luminosity, morphology, and host-galaxy properties, is consistent with observed spectral ages maps of radio lobes, and is able to reconcile the discrepancy between spectral and dynamical ages in powerful radio galaxies. In this way, the temporal evolution of a radio source can be modelled for, amongst other intrinsic properties, any combination of source age, jet kinetic power, and intergalactic environment (forward modelling hereafter).

Quantifying an AGN environment requires knowledge of the distribution of gas in the associated dark matter halo. Ideally this is done by constraining a gas density and temperature profile through X-ray observations, however such observations are largely unavailable across the majority of haloes, especially at higher redshifts. Turner & Shabala (2015) showed that estimates of the halo mass of the intergalactic environment can alternatively be inferred from the optically observed stellar content based on outputs of semi-analytic galaxy evolution models (e.g. SAGE; Croton et al. 2006); however, the shape of the gas density profile remains unconstrained by this method. RAiSE therefore quantifies the intergalactic environment in one of two ways: (1) by directly specifying a gas-density profile; or (2) by providing a mass of the dark matter halo, distributing the total gas mass based on an observationally based gas density profile

reported by Vikhlinin et al. (2006). In the latter example, this can be done based on either the mean profile or by randomly sampling a distribution of environment profiles from a galaxy formation model.

RAiSE implements a lobe emissivity model that considers radiative losses due to synchrotron radiation and the inverse-Compton upscattering of CMB photons, as well as the adiabatic losses related to the expansion of the lobes. This emissivity calculation is applied to small packets of electrons that are shock-accelerated at different points in the evolutionary history of the lobe. As a result, RAiSE considers the temporal evolution in the magnetic field, i.e. from the time electrons are shock-accelerated to the time they release their energy as synchrotron radiation. The magnetic field strength is derived from the lobe dynamics by assuming a constant ratio between the energy densities in the magnetic field and particles, referred to as the equipartition factor.

Over the past decade, models describing these processes have been incrementally added to the RAiSE code. Turner & Shabala (2015) provided the original implementation of a radio source model within a semi-analytic environment, and correspondingly modified the synchrotron emissivity model for the lobes. Turner et al. (2018a) used hydrodynamical simulations to spatially map the synchrotron emissivity across the lobes, allowing them to produce surface brightness maps of simulated radio sources; their model implemented tracer particles from hydrodynamical simulations to probe the average locations and ages of injected particles. Turner (2018) extended the dynamical and synchrotron emissivity models to account for the remnant phase during which the jets are inactive. Of relevance to this work, the dynamics presented by Turner & Shabala (2020) offer a slight modification to include the effect of a shocked gas shell.

The latest version of the RAiSE code,[6] as used in this work, is informed by the dynamics of Turner & Shabala (2020), and implements the method of Turner et al. (2018a) to produce intensity maps based on tracer particles from the higher resolution hydrodynamical simulation of Yates-Jones et al. (2022). Using individual hydrodynamical simulation particles rather than population averages enables RAiSE to synthesize hydrodynamical-based, high-resolution maps of the radio lobes at any observing frequency (see e.g. Fig. 5).

4.1.2 Constraining a RAiSE model

The RAiSE model is characterized by a variety of model parameters that represent intrinsic parameters of a radio source. These parameters are constrained in one of three ways: (1) through a direct measurement (e.g. injection index); (2) a prior probability distribution based on measurements of well-studied objects (e.g. ambient density profile); or (3) by way of a parameter inversion based on simulated observable attributes (e.g. jet power and age from size and luminosity).

RAiSE-based parameter inversions have been implemented by several previous authors to constrain the energetics of radio-loud AGNs. Turner & Shabala (2015) demonstrated the ability to recover the jet powers and lifetimes of radio sources using only their observed physical size and monochromatic radio luminosity; in their work, halo masses for each source were inferred from the stellar masses of their hosts using SAGE, and intrinsic parameters such as the equipartition factor and injection index were fixed to typical values. Turner et al. (2018b) were additionally able to recover the lobe equipartition factors by including the break frequency as an
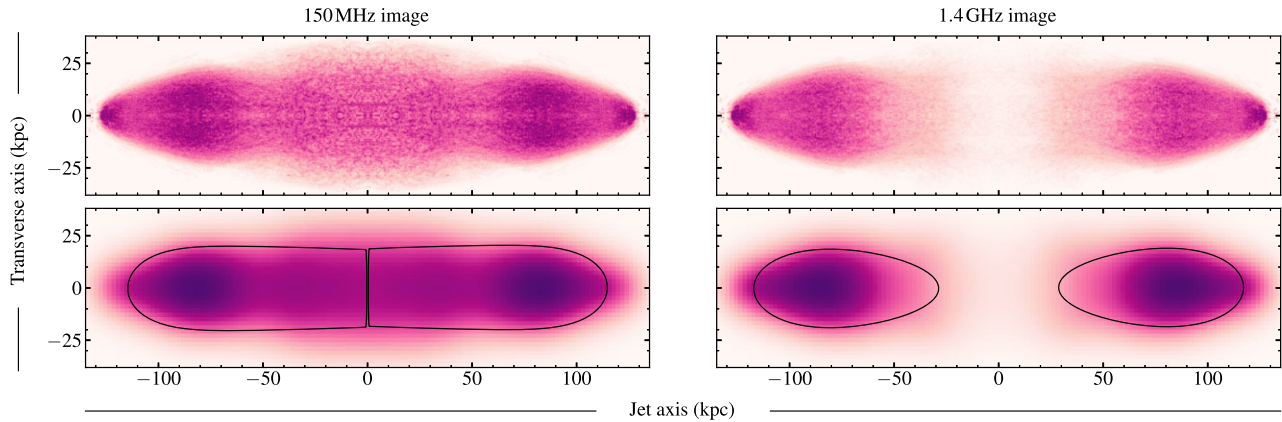
---

[6]https://github.com/rossjturner/RAiSEHD

Figure 5. Intensity maps predicted by RAiSE for a redshift $z = 0.1$ radio source with a jet-power of $Q = 10^{38}$ W, source age of $\tau = 100$ Myr, and a remnant ratio of $R_{rem} = 0.25$. The radio source is shown for 150 MHz (left-hand panels) and 1.4 GHz (right-hand panels), each of which is shown for a native resolution corresponding to 1.024×10^8 particles (upper panels) and for a convolved 10 arcsec image (lower panels). The pixel scale in the convolved image is 1 arcsec. Following the method outlined in Section 4.2.2, the observed surface brightness distribution is optimally fit by a skewed two-dimensional Gaussian; this is shown by a solid black contour, which represents the edge bounding 95 per cent of the Gaussian volume. Images of each fitted Gaussian are truncated at the core, resulting in the apparent abrupt cut-off at 150 MHz.

observational constraint. Turner et al. (2020) demonstrated that using only a reference flux density, angular size and width, break frequency and injection index, the cosmological redshift of radio sources can be constrained from the present epoch to the early-universe.

These results underline that the constraining power of the RAiSE-based parameter inversion is primarily limited by the input set of observational constraints. It is worth nothing that previous such applications of the RAiSE model have used attributes measured from observations with poor resolution. The capabilities of the current RAiSE model create a new opportunity to constrain intrinsic radio source parameters using additional attributes related to the observed surface brightness distribution of radio lobes. In the following sections, we exploit this opportunity to explore a new method for modelling the energetics of remnant AGNs.

4.2 The surface brightness distribution of radio lobes

In the absence of detailed spectral modelling, alternative constraints are needed to aid the modelling of the energetics of remnant AGNs. Here, we propose that the backflow of plasma in radio galaxy lobes offers such constraints, and subsequently develop a tool to parametrize the observed surface brightness distribution of radio lobes.

4.2.1 Constraints embedded in the lobe backflow

The plasma contained within FR-II radio lobes is injected throughout the active phase at the hotspot, and is carried away from the hotspot by the backflow (e.g. Turner et al. 2018a). This leads to a gradient in age across the lobes, *generally* in the form of an approximately linear increase in spectral age away from the hotspot. The observed shape of the emitting regions will vary depending on observing frequency; the low-frequency radiation produced by older electrons results in wider emitting regions along the jet-axis and transverse-axis, whereas at higher frequencies the bias towards observing younger electrons results in narrower emitting regions localized near the injection site. This is demonstrated in Fig. 5. Importantly, the manner by which the observing frequency modifies the observed spatial distribution of synchrotron-emitting electrons should depend on factors such as

the plasma age distribution and lobe magnetic field strength. In the absence of spectral modelling, it is therefore reasonable to suggest that well-resolved observations of remnant radio lobes should offer the constraints necessary to help disentangle their active and remnant time-scales.

4.2.2 Skewed two-dimensional Gaussian lobes

We require attributes to describe the observed surface brightness distribution of radio lobes, which can be compared between observations and simulations. We note that the reproduction of fine details is neither important nor captured by the RAiSE simulations (e.g. knots in the jets, or slight bending of the jets). Implementing a skewed Gaussian in two spatial dimensions is appropriate for the following reasons: (1) a Gaussian is able to describe the fall-off in brightness as a function of position; (2) in two dimensions, a Gaussian is able to characterize a measure of length of the lobe along the jet-axis, as well as a width along the transverse-axis; (3) introducing a 'skew' term along the major axis handles the asymmetry in brightness along the jet-axis (e.g. emission is typically brightest near the hotspot and falls off asymmetrically in each direction). In this way, the vastly different morphologies of, for example, a high-powered radio source (with a sharp fall-off in brightness away from the hotspot) and a low-powered aged remnant (with relatively smooth surface brightness profiles) can be characterized in a manner that is consistent.

To fit the skewed Gaussian to the observed surface brightness distribution of a radio lobe, the following free parameters are necessary:

(i) S_0, the amplitude of the Gaussian;
(ii) μ_x and μ_y, the coordinates of the peak amplitude in each dimension;
(iii) σ_x and σ_y, the standard deviation in each dimension;
(iv) θ, the major axis position angle;
(v) β_x, the skew term along the Gaussian major axis.

Since RAiSE simulates a jet in an known orientation and positions the SMBH at the centre of the image, the angle of rotation ($\theta = 0$) and μ_y are set by default (and therefore do not need solving). A simple least-squares algorithm is used to optimize the fit by minimizing
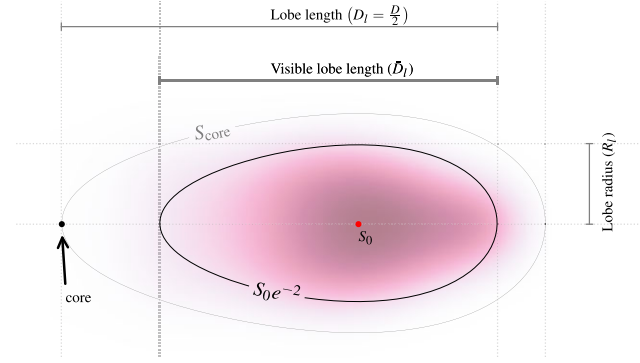
Figure 6. Schematic showing the key quantities necessary for computing the spatial attributes described in Section 4.3.1. The semitransparent purple emission represents the right lobe of the 1.4 GHz convolved image from Fig. 5. A skewed two-dimensional Gaussian is fit to the lobe surface brightness distribution following the method outlined in Section 4.2.2, where S_0 gives the amplitude of the fit. A solid black contour denotes the fitted Gaussian at a critical brightness level of $S_0 e^{-2}$, and bounds 95 per cent of the Gaussian volume.

the residuals between the radio lobe surface brightness distribution and Gaussian model. For stability, regression is performed to the square-root of the input image; this ensures fitting to the general shape, and down-weights bias towards the brightest pixels. The resulting Gaussian fit can then be used to parametrize key attributes related to the observed surface brightness distribution of a radio lobe (see Section 4.3.1 below). We make this code publicly available on GitHub.[7]

4.3 Radio source attributes

In this work, radio source attributes refer to the observable quantities that describe either the spatial, photometric, or spectral properties of radio galaxy lobes. By implementing these attributes in a RAiSE-based parameter inversion, they facilitate the comparison between observed radio sources and those simulated by the RAiSE model. However, images of real radio sources are 'degraded' by the sensitivity and resolution of the observations; degrading simulated images with these same observing limitations therefore enables a more meaningful comparison. In the following section, we describe the methods for measuring these attributes from observed and simulated images.

4.3.1 Spatial attributes

Spatial attributes are measured based on the Gaussian fitting method described in Section 4.2.2. We do this by first considering the boundary of the 2D ellipse formed by slicing the fitted Gaussian at some critical brightness level (see e.g. Fig. 5). We define this critical level as $S_0 e^{-2}$, above which 95 per cent of the Gaussian volume is contained. We stress that the arbitrary selection of this value does not matter; instead, what is important is that the same value is used when comparing both observed and simulated radio images, such that the resulting attributes are measured consistently. The following distances are measured by considering the boundary of the 2D ellipse (Fig. 6): the length of the lobe, D_l; the visible length of the lobe, $\bar{D}_l$; and the radius of the lobe, R_l. We consider the backflow in each lobe

[7] https://github.com/benjaminquici/skewed-Gaussian-lobes

Table 3. Spatial attributes evaluated using the quantities shown in Fig. 6.

Spatial attribute	Symbol	Expression	Limit
Linear size	D	$D_l^{\mathrm{lobe1}} + D_l^{\mathrm{lobe2}}$	–
Observed axial ratio	A	D_l/R_l	≥ 1
Extent 1	E	$D_l/\bar{D}_l$	0–1
Extent 2	$\bar{E}$	S_{core}/S_0	0–1

separately, and thus bound the visible lobe length as $0 < \bar{D}_l \leq D_l$. From here, we define four key spatial attributes, including the linear size, D, and observed axial ratio, A, as shown in Table 3.

Importantly, to constrain the duration of the remnant phase we develop two new measures of 'extent', which parametrize the observed backflow of lobe plasma. The 'extent 1' attribute, E, considers what fraction of the total lobe length, parallel to the jet axis, is visible, e.g. how far back the lobe visibly sweeps towards the core. Lobes with emission localized near the hotspot will measure $E \to 0$, which is expected if a majority of the lobe plasma energy is stored in the most freshly injected electrons. Conversely, $E \to 1$ implies the observed radio emission sweeps all the way to (and beyond) the core, which is expected if a majority of the lobe plasma energy is stored in the older synchrotron-emitting electrons. The 'extent 2' attribute, $\bar{E}$, considers how bright the lobes are at the core, relative to their peak brightness. We expect this attribute to be particularly useful at disentangling sources with backflow observed all the way to the core, where the measurement of the 'extent 1' attribute will likely just reflect its upper limit of $E = 1$.

4.3.2 Photometric attributes

A total radio luminosity, L_ν, offers a powerful constraint on radio source energetics. For an observed radio source, the total radio luminosity can be derived from the total radio flux density by integrating over a region of the source bounded by a minimum brightness criterion, e.g. the region of the source above some signal-to-noise threshold. This means that, for a fixed sensitivity, the measured integrated flux density will depend on the surface brightness distribution of the lobes. The surface brightness maps produced by the RAiSE model allow us to include the effect of instrumental noise in the computation of the integrated flux density, thus accounting for this systematic bias. This is done by populating the simulated surface brightness maps with a Gaussian noise term, then the total observed radio luminosity is calculated considering only pixels brighter than 3σ (where σ represents the level of Gaussian noise). This process of adding the noise is repeated over 16 iterations to sample a mean integrated flux density, and to characterize an uncertainty, dL_ν, based on the standard deviation across each evaluation.

By measuring the integrated flux density over two observing frequencies, ν_0 and ν_1, a two-point spectral index can be calculated through

$$\alpha = \log(L_{\nu,1}/L_{\nu,0})/\log(\nu_1/\nu_0), \tag{10}$$

which has an uncertainty corresponding to

$$d\alpha = \left(1/\ln(\nu_0/\nu_1)\right) \sqrt{(dL_{\nu,0}/L_{\nu,0})^2 + (dL_{\nu,1}/L_{\nu,1})^2}. \tag{11}$$

With at least three observing frequencies a spectral curvature, SPC, can be calculated through SPC $= \alpha_0 - \alpha_1$, which has an uncertainty corresponding to dSPC $= \sqrt{(d\alpha_0)^2 + (d\alpha_1)^2}$.

4.3.3 Spectral modelling attributes

The injection index and remnant ratio attributes, derived from observations by modelling the spectra of remnant radio galaxy lobes (Section 3), represent intrinsic parameters of the RAiSE model. On the other hand, a break frequency can be predicted by the RAiSE model, which offers valuable constraints on the lobe equipartition factor. While it is possible to measure a RAiSE-predicted break frequency by modelling a simulated radio spectrum, the computational cost of simulating a radio source at many different frequencies makes this method inefficient. For any given set of model parameters, the RAiSE code uses the lobe pressure and equipartition factor to compute the lobe magnetic field strength. In turn, the field strength is used through equation (3) to calculate the corresponding RAiSE-predicted break frequency, where the redshift and source age are those used as RAiSE model inputs. By modelling the spectra of RAiSE-simulated radio sources, Turner et al. (2018b) showed that the break frequency computed from the magnetic field strength is consistent with that derived by modelling their synthetic radio spectra (see e.g. their fig. 3).

4.4 Modelling the energetics of J2253-34

We are now equipped with the tools needed to model the energetics of J2253-34. To begin with, we model the energetics closely following the dynamical-model-based method presented by Turner (2018). Here, the remnant ratio is already known (e.g. from Section 3.4.2), while the jet power, source age, and equipartition factor are principally constrained from a radio luminosity, physical size, and break frequency. We compare this established technique to our proposed method using the spatial attributes of the lobes (namely extent) to additionally constrain the remnant ratio. Finally, we provide our most precise constraints on the energetics by combining both the spectral and spatial attributes to best understand the physics of J2253-34.

4.4.1 Observed properties of J2253-34

The radio galaxy J2253-34 was classified as a remnant by Quici et al. (2021) based on the absence of radio emission from the core, and further supported by the observed steepening in the integrated radio spectrum. In that work, the radio source was unambiguously associated with a $z = 0.2133$ host galaxy, for which a halo mass of $M_{\rm H} = 10^{13.5}\,{\rm M}_\odot$ was inferred based on the stellar mass of the host.

The radio source attributes of J2253-34 are measured following the methods outlined in Section 4.3, and are summarized in Table 4. All spatial attributes are measured from the 8 arcsec images presented in Section 2, and we use the injection index, break frequency, and remnant ratio fitted in Section 3.4 by the Tribble spectral ageing models (e.g. rows 2 and 4 of Table 2). In the following section, we implement these attributes to constrain the energetics of J2253-34 via a parameter inversion.

4.4.2 RAiSE-based parameter inversion of J2253-34

RAiSE can model the temporal evolution of radio lobes for any set of intrinsic radio source parameters, and subsequently generate mock images to make predictions for their respective radio source attributes. The intrinsic parameters of any radio source can therefore be estimated via a RAiSE-based parameter inversion; observed radio source attributes are compared to a corresponding set of mock attributes generated over a multidimensional set of intrinsic

parameters (e.g. as is done by Turner & Shabala 2015; Turner 2018; Turner et al. 2018b; Shabala et al. 2020).

For a fixed redshift of $z = 0.2133$ and halo mass of $M_{\rm H} = 10^{13.5}\,{\rm M}_\odot$, a grid of RAiSE models are created from the two-sided jet kinetic power, Q; the dynamical source age, τ; the equipartition factor, q (which parametrizes the ratio of energy densities in the magnetic field and particles; Turner et al. 2018a); the initial supersonic phase value of the axial ratio, A_i; the remnant ratio, $R_{\rm rem}$; and the injection index, s. We use the results of Turner et al. (2018b), who fit the intrinsic properties of 3C radio sources, to ensure our model grid covers plausible parameter values. In this work, RAiSE models are evolved between 10 Myr to 1 Gyr, recording outputs at every $\Delta(\log \tau) = 0.05$ dex. We uniformly sample $\log Q$ in the range [37, 40] with a precision of 0.05 dex; $\log q$ in the range [−2.7, −0.7] with a precision of 0.05 dex; A_i in the range [2, 8] with a precision of 0.25; $R_{\rm rem}$ in the range [0, 5] with a precision of 0.01; and s in the range [2.01, 2.61] with a precision of 0.1.

To explore the constraining power of the extent attributes, we perform the parameter inversion based on four separate combinations of the radio source attributes, summarized in columns 5–8 of Table 4. The SPATIAL method tests a scenario where detailed spectral modelling (e.g. Section 3.4) cannot be performed; here, each intrinsic radio source parameter is explicitly fit via the RAiSE-based parameter inversion, and the break frequency is omitted as a constraint. To independently verify results of this method, the fitted energetics are compared with that fitted by the FULL FIT and SPECTRAL methods; here, the injection index and, importantly, the remnant ratio are fixed to known values, and the strong constraint from the break frequency is included. The IN BAND method considers a limiting case where no constraints on the duration of the remnant phase are available.

To conduct the parameter inversion (for any of the above methods), simulated images are used to measure the same attributes as those measured for J2253-34, ensuring that the images are degraded by the same set of observing constraints. Attributes are compared with model outputs through equation (9), and we follow the same process described in Section 3.2 to select the best-fitting model, and to estimate the uncertainty in each parameter.

The values fitted for the intrinsic parameters using each of these methods are presented in Table 5. Consistent with the results of Turner (2018), we find that the jet-power/age/equipartition-factor triplet, fitted by the SPECTRAL method, is tightly constrained by the observed radio-luminosity/linear-size/break-frequency. We inspect the marginal distributions of each fitted parameter to find approximately Gaussian-like PDFs centred about the peak probable value, i.e. the fitting appears stable and not degenerate. By including constraints from the extents, we find that the energetics constrained by the FULL FIT method do not change. This suggests that the break frequency is the dominant observable in this fitting process.

Using the source age constrained by FULL FIT method, together with the remnant ratio fit previously by the TCI model, the duration of the active and remnant phases in J2253-34 are calculated as $t_{\rm on} = 43.3 \pm 4.3$ Myr and $t_{\rm rem} = 12.9 \pm 1.2$ Myr, respectively. Importantly, through this method we demonstrate the ability to accurately measure the duration of the active phase, and to place a weak upper bound on the AGN jet duty cycle ($\delta \lesssim 1 - R_{\rm rem} = 0.77$).

Remarkably, we find that the energetics modelled by the SPATIAL method are consistent with those derived by the previous methods. Uncertainties in each parameter are comparatively greater, as expected considering the constraints are relaxed and an additional free parameter is solved for, however inspecting the marginal distributions reveals similar Gaussian-like PDFs. What is particularly of interest

Table 4. The measured radio source attributes of J2253-34, which are measured following the methods outlined in Section 4.3. In Section 4.4.2, these attributes are compared with corresponding RAiSE model outputs, using the scale shown in column 4, to constrain the energetics via a parameter inversion. To explore the constraints embedded in the lobe backflow, attributes are compared in four different combinations (columns 5–8). Tick (✓) and cross (✗) markers represent whether the attributes are included or excluded from the fitting, respectively.

Radio source attribute	Symbol	Measurement	Scale	FULL FIT	SPECTRAL	SPATIAL	IN BAND
Radio luminosity (measured at 1.42 GHz)	$L_{1.4}$	$(6.48 \pm 0.25) \times 10^{24}\,\mathrm{W\,Hz^{-1}}$	$\log_{10}$	✓	✓	✓	✓
Largest linear size (measured at 1.42 GHz)	$D_{1.4}$	326 kpc	$\log_{10}$	✓	✓	✓	✓
Break frequency	ν_b	$1.26^{+0.06}_{-0.05}$ GHz	$\log_{10}$	✓	✓	✗	✗
Observed axial ratio (1.42, 5.50 GHz)	$A_{1.4}, A_{5.5}$	$2.4 \pm 0.1, 2.7 \pm 0.1$	linear	✓	✓	✓	✓
Extent 1 (1.42, 5.50 GHz)	$E_{1.4}, E_{5.5}$	$0.9 \pm 0.05, 0.8 \pm 0.05$	linear	✓	✗	✓	✗
Extent 2 (1.42, 5.50 GHz)	$\bar{E}_{1.4}, \bar{E}_{5.5}$	$0.76 \pm 0.05, 0.65 \pm 0.05$	linear	✓	✗	✓	✗
Spectral index (150−1420) MHz	α_{150}^{1420}	0.64 ± 0.03	linear	✗	✗	✗	✓
Spectral curvature (150−1420−5500) MHz	$\mathrm{SPC}_{150}^{5500}$	0.53 ± 0.04	linear	✗	✗	✗	✓

Table 5. The intrinsic parameters of J2253-34, constrained via the four separate methods outlined in Table 4.

Param.	FULL FIT	SPECTRAL	SPATIAL	IN BAND
Q ($\times 10^{38}$ W)	$3.98^{+0.36}_{-0.40}$	$3.98^{+0.36}_{-0.40}$	$6.32^{+2.11}_{-1.63}$	1.0–7.9
τ (Myr)	$56.2^{+2.62}_{-1.28}$	$56.2^{+2.62}_{-1.28}$	$50.1^{+4.2}_{-3.8}$	31–158
B ($\times 10^{-10}$ T)	$1.98^{+0.16}_{-0.15}$	$1.98^{+0.16}_{-0.15}$	$1.41^{+0.30}_{-0.25}$	2–14
$R_{\rm rem}$	$^\dagger 0.23^{+0.02}_{-0.02}$	$^\dagger 0.23^{+0.02}_{-0.02}$	$0.26^{+0.04}_{-0.03}$	0.1–0.3

Note. †parametrized by the CI model.

is that the dynamically modelled remnant ratio, $R_{\rm rem} = 0.26 \pm 0.02$, is consistent with that parametrized by the TCI model within a level of 1σ. Together with a source age of $\tau = 50.1^{+4.2}_{-3.8}$ Myr, the SPATIAL method therefore estimates the duration of the active and remnant phases as $t_{\rm on} = 37.2 \pm 4.3$ Myr and $t_{\rm rem} = 13.1 \pm 1.5$ Myr, respectively. These time-scales are consistent with those fitted by the FULL FIT method, suggesting that the surface brightness distribution of the lobe backflow can in fact be used to constrain the dynamics of the remnant phase.

Finally, we find that the stability of the model fitting breaks down severely with the IN BAND method. Inspecting the marginal distributions reveals a large degeneracy in the fitted parameter space, where multiple unique values of equal likelihood are found over a wide range of parameter values. We quote these ranges in Table 5, by considering their minimum/maximum values. This tells us that the spectral index and curvature, alone, do not offer the constraining power needed to tightly constrain the energetics of J2253-34.

5 MOCK RADIO SOURCE POPULATIONS

The ability to measure the off-time in remnant radio galaxies, using attributes measured exclusively below $\sim$1.4 GHz, is particularly attractive considering the parameter space unlocked by wide-area sky surveys such as the LOFAR Two-metre Sky Survey (LoTSS; Shimwell et al. 2019, 2022), the MeerKAT International GHz Tiered

Extragalactic Exploration (MIGHTEE; Jarvis et al. 2016) survey, the APERture Tile In Focus (Apertif Oosterloo, Verheijen & van Cappellen 2010) survey, and EMU. However, the generalizability of this new method is currently unclear, as we do not know whether the constraining power of the spatial attributes, measured using telescope-degraded images, deteriorates for certain intrinsic source parameters, e.g. lower jet powers, older sources, or denser environments. In Section 5.1, we use our method to perform a parameter inversion of mock radio source populations simulated at 150 MHz and 1.4 GHz. In Section 5.2, we compare the input and recovered parameters to examine the internal consistency of our method within the RAiSE model, e.g. does the method recover the input parameters. In Section 5.3, we then examine whether the remnant ratio fitted by this method can be used to confidently select between active and remnant radio lobes.

5.1 Constructing mock radio source catalogues

For this analysis, mock radio source populations are simulated using the RAiSE model. We allow the following set of intrinsic parameters to vary over a wide range of values, typically associated with FR-IIs:

(i) *jet power:* $Q \in [10^{37},\ 10^{40}]$ W, to represent those typically associated with FR-II jets (Turner & Shabala 2015)

(ii) *source age:* $\tau \in [10^7,\ 10^{8.5}]$ yr. Younger sources will likely fall below extended source criteria (see Fig. 7), and a genuine dearth of old ($>$400 Myr) radio sources has been reported by Shabala et al. (2020) in LOFAR data.

(iii) *remnant ratio:* $R_{\rm rem} \in [0, 0.5]$, consistent with the observational bias towards selecting recently switched-off remnants (Mahatma et al. 2018; Turner 2018; Jurlin et al. 2020; Shabala et al. 2020; Quici et al. 2021).

(iv) *equipartition factor:* $q \in [10^{-2.7}, 10^{-0.7}]$, which is approximately Gaussian-distributed about $\log q \approx -1.7$ (see e.g. Turner et al. 2018b).

(v) *initial axial ratio:* $A_i \in [2.5, 4.5]$, reflecting a subset of typical values for the 3C sample (see e.g. Turner & Shabala 2015).

(vi) *injection index:* $s \in [2.01, 2.61]$, where the lower limit comes from predictions of first-order Fermi acceleration (Kardashev 1962; Pacholczyk 1970), and the upper limit from $\alpha_{\rm inj}$ not being too steep.
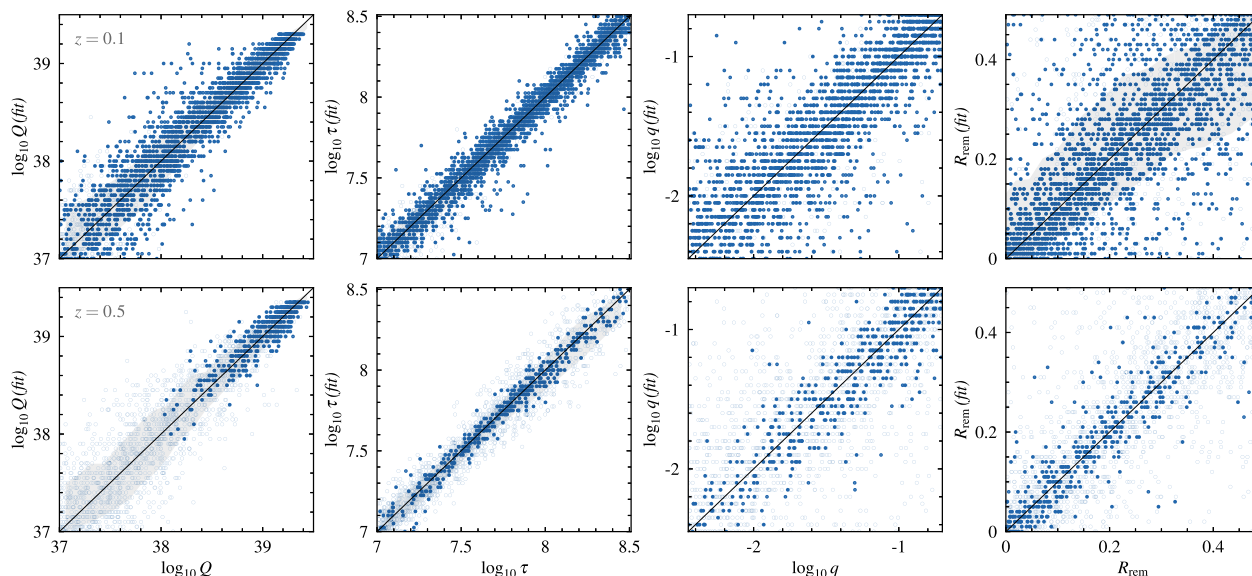
Figure 7. Results of the parameter inversion of the $z = 0.1$ (upper row) and $z = 0.5$ (lower row) mock catalogues are shown. Each plot demonstrates the fitted (vertical axis) versus mock (horizontal axis) parameter for the jet power (first column), source age (second column), equipartition factor (third column), and remnant ratio (fourth column). Each marker represents a unique mock radio source, where unfilled markers represent sources fainter than $S_{150} = 100$ mJy or smaller than $\theta = 60$ arcsec. A solid black line is shown to represent a 1:1 relation between the fitted and mock quantities.

Table 6. The set of observing conditions used to sample mock radio source populations simulated in Section 5.1.

Survey type	Freq. (MHz)	Sensitivity (μJy beam^{-1})	Resolution (arcsec)
LOFAR-like *(wide-band)*	150	70	6
LOFAR-like *(sub-band)*	130 170	100	6
MeerKAT-like	1400	6	10

Table 7. The set of radio source attributes used to constrain the energetics of the mock radio source populations described in Section 5.1.

Attribute	Scale
150 MHz radio luminosity	$\log_{10}$
Largest linear size	$\log_{10}$
Observed axial ratio (150, 1400) MHz	linear
Extent 1 (150, 1400) MHz	linear
Extent 2 (150, 1400) MHz	linear
(150–1420) MHz spectral index	linear
(150–1420) MHz spectral curvature	linear

Two separate mock catalogues are created at redshift $z = 0.1, 0.5$ (hereafter the $z = 0.1$ and $z = 0.5$ catalogues). For each catalogue, 5000 mock radio sources are forward modelled using pseudo-random values for the intrinsic parameters. We use a representative $M_{\rm H} = 10^{13}$ M$_\odot$ halo mass (e.g. a typical environment of an FR-II, Turner & Shabala 2015), and simulate a random gas-density profile based on a prior distribution of environment profiles (as per discussion in Section 4.1.1).

A corresponding grid of RAiSE models is simulated with known values for each intrinsic parameter, so that a parameter inversion can be performed on each mock radio source catalogue. Our model grids are bound by the parameter space limits of the mock sample, however with uniform spacings as follows: $\Delta(\log Q) = 0.05$ dex; $\Delta(\log \tau) = 0.025$ dex; $\Delta R_{\rm rem} = 0.01$; $\Delta(\log q) = 0.05$ dex; $\Delta A_i = 0.25$; and $\Delta s = 0.1$. Sources are simulated for the same halo mass, however here we take the mean of the environment profiles.

Bayesian parameter estimation is conducted as follows. Images are synthesized at 150 MHz and 1.4 GHz, and degraded by a set of survey limitations shown in Table 6. This is done both for mock radio sources and those stored in the grid as model outputs. Telescope-degraded images are then used to measure the radio source attributes shown in Table 7. Following the parameter inversion described in Section 4.4.2, the attributes

measured for mock radio sources are compared with those used as model outputs, in order to constrain their intrinsic parameters. Here, we simultaneously fit for the pseudo-randomly sampled parameters, and treat the redshift and halo mass as known.

Sources are flagged if their angular size falls below $\theta = 60$ arcsec, or if their 150 MHz integrated flux densities fall below $S_{150} = 100$ mJy. This decision is motivated by the typical current observational constraints used to construct complete radio galaxy samples (e.g. Brienza et al. 2017; Godfrey et al. 2017; Mahatma et al. 2018; Jurlin et al. 2020; Quici et al. 2021). The results of this parameter inversion are explored in the following sections.

Finally, we note that the Karl G. Jansky Very Large Array Sky Survey (VLASS; Lacy et al. 2020) represents a high-frequency (2–4 GHz), high-resolution (2.5 arcsec), all-sky (Dec. > −40°) radio survey, which is expected to achieve $\sigma = 70$ μJy beam^{-1} sensitivity. Despite marginally increasing the frequency leverage over 1.4 GHz, we do not consider a VLASS-like observation due to the comparatively poorer surface brightness sensitivity to extended radio emission; without a handle over the fainter (older) lobe electrons, we expect the observed backflow to be much less constraining on the remnant off-time.
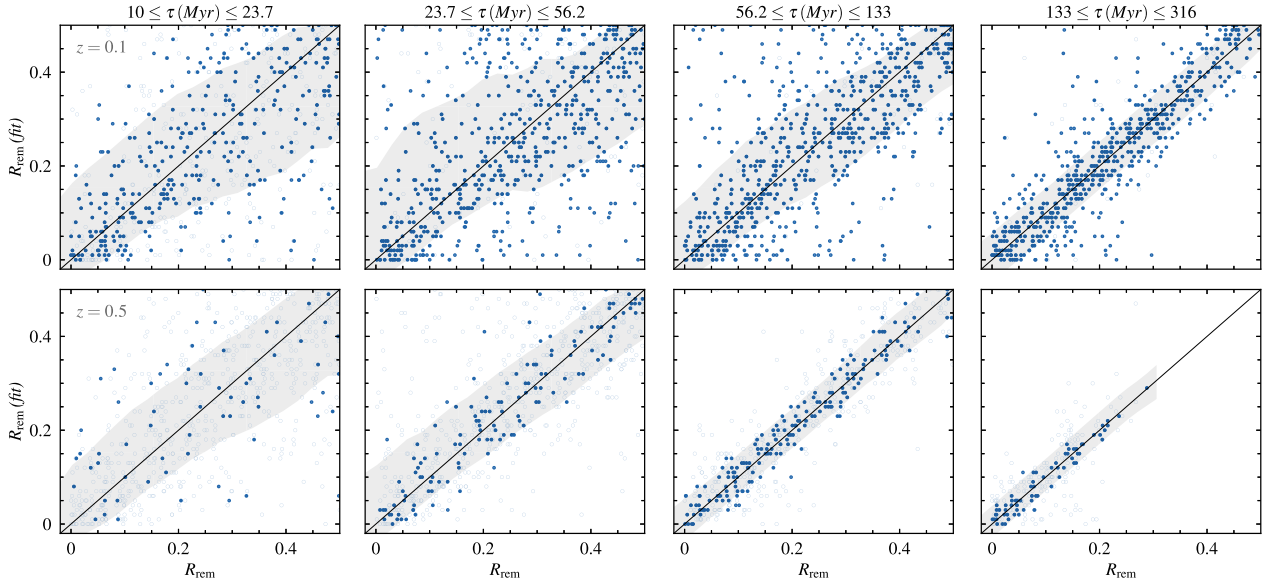
Figure 8. The fitted (vertical axes) versus input (horizontal axes) remnant ratio of the $z = 0.1$ (upper panel) and $z = 0.5$ (lower panel) mock catalogues. Each column represents a log-uniform source age bin. The grey regions represent a 1σ uncertainty in the scatter, corresponding to the unflagged sources (filled markers). A tightening in the scatter is seen as the source age increases, likely reflecting the greater magnitude of radiative losses discussed in Section 5.2. The dearth of sources with higher values of $R_{\rm rem}$ in the $z = 0.5$ sample arises due to the complete depletion of electrons capable of producing emission at these frequencies (see e.g. fig. 4 of Turner 2018).

5.2 Fitted energetics

We expect that the parameter inversion may be less effective for some sets of parameters due to the non-linear application of radiative losses across our parameter space. In particular, the two extent attributes, and to a lesser degree the lobe width attribute, rely on the surface brightness distribution of ageing synchrotron-emitting lobe plasma. The ageing is quantified through the time derivative of the Lorentz factor of a given packet of synchrotron-emitting electrons, γ, as follows (Kaiser, Dennett-Thorpe & Alexander 1997):

$$\frac{d\gamma}{dt} = -\frac{a_1\gamma}{3t} - \frac{4\sigma_T\gamma^2\,(u_B + u_C)}{3m_e c}, \qquad (12)$$

where the first and second terms encode adiabatic and radiative losses, respectively. Here, the derivative is taken with respect to the age of the injected plasma, t, where a_1 gives the exponent with which the volume of the lobe grows adiabatically, σ_T is the cross-section for Thompson scattering, and u_B and u_C are the energy densities of the magnetic field and CMB, respectively.

Comparisons between their mock and fitted intrinsic parameters are presented in Fig. 7 for the two mock catalogues described in Section 5.1. First, although with varying degrees of confidence (as indicated by the scatter), we find that the fit of each parameter broadly closely matches the 1:1 relation with its mock equivalent. The jet power and source age are fit with greater confidence than the equipartition factor and remnant ratio, demonstrating the former two property's dependence on observable parameters, e.g. the jet power and source age are tightly constrained by the radio luminosity and linear size, respectively, at least for active lobed sources (Turner & Shabala 2015). However, it is encouraging to find that the equipartition factor and remnant ratio are generally recovered as well.

The jet power is less confidently predicted using the RAiSE-based parameter inversion for lower powered sources, as shown in Fig. 7. This is unlikely a selection effect, in which the stochastic

perturbations due to instrumental noise are more significant for fainter sources associated with lower powered jets, since the same sizeable broadening is observed in the $z = 0.1$ (brighter) catalogue. Instead, this is likely due to the strong correlation between jet power and the lobe magnetic field strength, and thus energy density u_B (see e.g. equation A5 of Turner et al. 2018a). The rate of energy loss from the synchrotron-emitting electrons is therefore expected to be much greater in higher jet power sources (equation 12), thus leading to a greater rate of change in the extent attributes as the remnant ages. Qualitatively, this is consistent with the results of Turner (2018), who find a rapid dimming in higher powered remnants in stark contrast to lower powered sources whose flux density is maintained over a greater duration (see their fig. 4).

We also find that the energetics of the $z = 0.5$ sample are fit with greater confidence (see also discussion in next paragraph). Again referring to equation (12), this result is unsurprising; the energy density of the CMB scales with redshift as $u_c \overset{\propto}{\sim} z^4$, meaning the magnitude of the energy losses sustained throughout the remnant phase will be greater.

We investigate if the sizeable scatter in the remnant ratio is partially due to one of the other model parameters. In particular, we expect the radiative losses in the remnant phase will be related to the off-time, rather fractional time spent in the remnant phase (e.g. integrating equation 12 for constant volume, i.e. $a_1 = 0$). As a result, we expect the synchrotron losses to reduce the extent attributes in approximate proportion to the time spent in the off-phase. The ability of the RAiSE-based parameter inversion to constrain the remnant ratio is therefore expected to correspondingly be much less effective in young sources (i.e. the off-time is smaller for a given remnant fraction). To consider this potential sensitivity in our method, we group the mock catalogues into four source age bins uniformly spaced in $\log\tau$. The fitted remnant ratio, in each source age bin, compared to the mock remnant ratio is presented in Fig. 8. We find that the scatter in the predicted remnant ratio reduces considerably for the older source age bins, as expected from the above discussion.

Overall, the results presented here show promise for modelling the energetics of remnant AGNs, and notably, using spatial attributes of their lobes to constrain the remnant phase. The predictive power of this technique improves when the magnitude of the energy losses sustained during the remnant phase are greater; this is unsurprising, as the technique relies on the reduction in extent to constrain the ageing during this phase. The method makes reliable estimates of the remnant ratio associated with older sources, in contrast to young sources for which the fitted remnant ratio is less trustworthy.

5.3 Identifying remnant radio galaxies

As we have demonstrated the ability of our method to estimate the remnant ratio with reasonable accuracy, this raises the question of whether we can use the same method to select remnant radio galaxies. Part of the difficulty here is ascertaining a definition for active and remnant sources based on the fitted remnant ratio parameter; logically, active sources would only correspond to $R_{rem} = 0$ (i.e. zero off-time), however in practice it would be impossible to distinguish a very recently switched-off source from an active source.

By creating mock radio source catalogues with known remnant ratios, we can use the distribution in the fitted remnant ratio to quantify the probability that: (1) an active radio source is fit with a non-zero remnant ratio; and (2) an 'unambiguous' (i.e. $R_{rem} \geq 0.1$) remnant radio source is fit with $R_{rem} = 0$. To do this, we follow the method outlined in Section 5.1 to create three mock catalogues per redshift. Each catalogue contains 5000 sources, and the remnant ratios are fixed at $R_{rem} = 0, 0.1, 0.2$, respectively. For each redshift and source age bin, we characterize the 68th and 95th percentiles of the fitted remnant ratio distribution; these serve as upper bounds for the $R_{rem} = 0$ catalogue, and lower bounds for the $R_{rem} \geq 0.1$ catalogues. An example of this is demonstrated in Fig. 9 for the highest source age bin at $z = 0.1$, and we summarize our results in Table 8 for all the redshift and source age bins.

We find that the recovery rate of active radio galaxies is high; in 95 per cent of the cases, the fitted remnant ratio is $R_{rem} \leq 0.1$ (the actual value being 0 per cent), which is true across all redshift and source age bins (column 4 of Table 8). We conclude similar results for the $R_{rem} = 0.1$ remnant radio galaxies; in 95 per cent of the cases, the fitted remnant ratio is $R_{rem} > 0.01$ (column 6 of Table 8), meaning that active sources are not contaminated by $R_{rem} = 0.1$ remnants, at this level. For example, if examining a sub-catalogue of $z = 0.1$ radio source with fitted ages of 133 to 316 Myr, we can confidently (at 2σ level) say that those with remnant ratio $R_{rem} < 0.03$ will not have significant contamination from 'unambiguous' remnants and can therefore be classified as active sources. Conversely, those objects with fitted remnant ratios $R_{rem} > 0.05$ will not have significant contamination from active sources and can be classified as remnants. We examine the same statistics for the $R_{rem} = 0.2$ sample, and reassuringly find no contamination of active sources from this population.

6 CONCLUSIONS

This paper investigates a new technique to constrain the energetics of remnant radio galaxies based on the backflow of their lobe plasma. We employ observations of the remnant radio galaxy J2253-34 together with mock radio source populations, in order to verify the method and examine its applications and limitations. The approach taken to explore this technique, and the insights gathered, are summarized below.
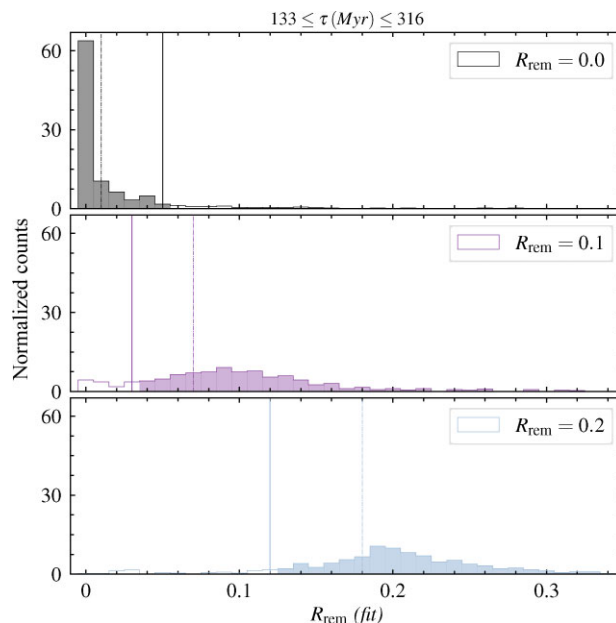

Figure 9. Normalized count representing the distribution of fitted remnant ratios of mock samples with $R_{rem} = 0$ (black), $R_{rem} = 0.1$ (purple), and $R_{rem} = 0.2$ (blue). We set the bin size in each distribution to $\Delta R_{rem} = 0.01$, to reflect spacings in the grid. Each sample is simulated at redshift $z = 0.1$, and only the oldest source-age bin ($133 \leq \tau \leq 316$) Myr is shown. The solid and dotted vertical lines are shown to represent the 68th and 95th percentiles in each sample, respectively; these represent upper bounds for the active population, and lower bounds for the remnant samples.

First, we use established spectral ageing techniques to derive a precise measurement of the off-time in J2253-34; this is needed to independently validate the results of our new method. To do this, we collect new radio observations using the MeerKAT, ATCA, and uGMRT telescopes (Section 2). The injection index is tightly constrained by jointly fitting the JP spectra arising from narrow regions across the lobes (Section 3.4.1). We then make precise measurements of the break frequency and remnant ratio by fitting the TCI model to the integrated radio lobe spectrum (Section 3.4.2); here, the previously fitted injection index is used as a model input. Our key results are summarized as follows:

(i) We develop a PYTHON implementation of synchrotron spectral ageing models, as well as algorithms to fit these models to observed radio data. We release this code, the SYNCHROFIT library, to the broader astrophysics community for its relevance to modelling the synchrotron spectra from active galaxies and supernovae remnants (Section 3.2).

(ii) To place the tightest constraints on the break frequency and remnant ratio, the injection index should be independently fit and used as an input on the CI model; this can be done by considering individual JP spectra across the lobes (cf. Shulevski et al. 2017).

(iii) The shape of the Tribble spectral ageing models is (at most) weakly dependent on the average magnetic field of the underlying Maxwell–Boltzmann distribution (Section 3.3). These models, which likely provide a more realistic treatment of a turbulent magnetic field, can therefore be fit to observed radio data without needing prior knowledge of the lobe magnetic field strength.

(iv) The remnant ratio in J2253-34 is tightly constrained as $R_{rem} = 0.23 \pm 0.02$.

Table 8. The recovery rate of active and remnant radio sources simulated in Section 5.3. Three mock radio source catalogues ($N = 5000$) are created at $z = 0.1$ and $z = 0.5$, with remnant ratios fixed to $R_{rem} = 0$, 0.1, 0.2, respectively. For each redshift (column 1) and source age bin (column 2), the 68th and 95th percentiles of the fitted remnant ratio distribution are reported (columns 3–8).

Redshift	Mock sample Source age (Myr)	Active (68th *perc.*)	(95th perc.)	Remnant ($R_{rem} = 0.1$) (68th perc.)	(95th perc.)	Remnant ($R_{rem} = 0.2$) (68th perc.)	(95th perc.)
$z = 0.1$	$10.0 \leq \tau < 23.7$	≤ 0.00	< 0.05	> 0.07	> 0.02	> 0.15	> 0.08
	$23.7 \leq \tau < 56.2$	≤ 0.00	< 0.12	> 0.07	> 0.01	> 0.15	> 0.06
	$56.2 \leq \tau < 133.0$	< 0.01	< 0.10	> 0.07	> 0.01	> 0.16	> 0.06
	$133.0 \leq \tau \leq 316.0$	< 0.01	< 0.05	> 0.07	> 0.03	> 0.18	> 0.12
$z = 0.5$	$10.0 \leq \tau < 23.7$	≤ 0.00	< 0.05	> 0.06	> 0.01	> 0.14	> 0.03
	$23.7 \leq \tau < 56.0$	≤ 0.00	< 0.03	> 0.08	> 0.05	> 0.17	> 0.13
	$56.2 \leq \tau < 133.0$	< 0.01	< 0.03	> 0.09	> 0.06	> 0.19	> 0.17
	$133.0 \leq \tau \leq 316.0$	≤ 0.00	< 0.02	> 0.09	> 0.08	> 0.19	> 0.18

Our new method utilizes the lobe surface brightness distribution to parametrize the backflow of plasma, and exploits the RAiSE dynamics and emissivity model. The high-resolution hydrodynamical simulation underpinning the RAiSE code enables the synthesis of mock surface-brightness maps, which are used to measure predicted radio source attributes. These are compared with observations so that the intrinsic source properties can be obtained via a parameter inversion. We apply this method to constrain the energetics of J2253-34, and obtain the following results:

(i) We propose two new attributes to quantify the spectral ageing of lobe plasma as it flows away from the hotspot towards the core. The 'extent 1' attribute considers how far back the lobe visibly sweeps towards the core, and the 'extent 2' attribute considers the surface brightness of the lobe at the core, relative to the peak surface brightness.

(ii) We implement a RAiSE-based parameter inversion using these two new attributes, in addition to the lobe radio luminosity, size, and axial ratio, to constrain a remnant ratio of $R_{rem} = 0.26 \pm 0.02$ for J2253-34. Importantly, this is consistent at the 1σ level with that constrained by our spectral fitting, verifying our approach to constrain the dynamics of the remnant phase based on the surface brightness distribution of the lobe backflow.

(iii) By comparing different sets of attributes, we find that the break frequency is the dominates the 'extent' attributes fitting of the energetics; particularly the equipartition factor and remnant ratio. By excluding the break frequency and extent attributes from the fitting, we find that the spectral index and curvature, alone, do not offer enough constraining power to uniquely fit the source energetics.

(iv) For J2253-34, we accurately measure a two-sided jet kinetic power of $Q = 3.98^{+0.36}_{-0.40} \times 10^{38}$ W, a lobe magnetic field strength of $B = 0.20 \pm 0.02$ nT, and importantly an active and remnant time-scale of $t_{on} = 37.2 \pm 4.3$ Myr and $t_{rem} = 13.1 \pm 1.5$ Myr.

We then used synthetic radio lobes, simulated for a typical 150 MHz LOFAR-like and 1.4 GHz MeerKAT-like observation, to further examine the limitations of our proposed method with respect to intrinsic radio source parameters. Our key results are summarized as follows:

(i) The jet power, source age, equipartition factor, and remnant ratio are consistently recovered, noting that the former two are constrained with high precision. This result builds on the work conducted by Turner et al. (2018b) for active sources only, who similarly find that the jet power, source age, and equipartition factor are constrained from the source size, radio luminosity, and break frequency.

(ii) Our results show that the parameters are more accurately fit for radio sources with higher redshifts, due to increased strength of IC losses; higher powered jets, due to increase in magnetic field strength; and for a greater duration of the remnant phase. We therefore find that the constraining power of our method increases when the magnitude of the energy losses, sustained during the remnant phase, are greater.

(iii) Remnant ratios fitted by this method can be trusted if the measured source age is large, and conversely, is less accurate for younger sources. To interpret the on/off-times fit by this method, one should first consider the age of the source to determine if the fitted remnant ratio is estimated reliably.

(iv) We find that our method is capable of selecting active and remnant radio galaxy candidates. At low redshift ($z \sim 0.1$), we find that sufficiently aged sources ($\tau > 50$ Myr) fitted with $R_{rem} \leq 0.1$ are active radio galaxies within a confidence of 95 per cent; this extends to sources as young as $\tau \sim 10$ Myr at higher redshifts ($z \gtrsim 0.5$). Similarly, we find that sources fit with $R_{rem} \geq 0.1$ are true remnant radio galaxies within a confidence of 95 per cent; these classifications are more robust at higher redshift.

The outcomes of this work show promising applications to studying the energetic impact of radio-loud AGNs on their environments, in particular, through studying remnant radio galaxies. However, although this method is clearly successful for remnants with $R_{rem} \lesssim 0.23$, for much older remnants the model assumptions in the version of RAiSE used in this work may no longer capture all the necessary physics, for example buoyancy and Rayleigh–Taylor instability; capturing these physical processes will be an important step necessary for modelling aged remnants, e.g. Blob 1 with $R_{rem} \sim 0.8$. Other complexities, such as dynamic or non-cluster-centred environments, can lead to asymmetries in the radio lobe morphologies, e.g. in jet lengths, as well as lobe luminosities. Hydrodynamical simulations of the jet and lobe evolution in such environments already exist (see Yates-Jones et al. 2021), which can incorporate the calculation of the resolved adiabatic and radiative loss processes following Yates-Jones et al. (2022). While the direct outputs of such hydrodynamical simulations can be implemented in the grid-based approach of this work, their synthesis is computationally expensive and can realistically only coarsely sample any given parameter space. The RAiSE framework can naturally consider asymmetries by allowing its governing differential equations for the source expansion to be applied on arbitrarily small solid angle elements; in this manner, future work can utilize modified versions of this code that include relevant physical processes to efficiently simulate millions of mock sources densely throughout the intrinsic parameter space.

ACKNOWLEDGEMENTS

DATA AVAILABILITY

The raw data products underlying Section 2 are available on the following data archives: the Australia Telescope Online Archive (ATOA) at https://atoa.atnf.csiro.au/ (Section 2.1); the South African Radio Astronomy Observatory (SARAO) Web Archive at https://archive.sarao.ac.za/ (Section 2.2); and the GMRT Online Archive (GOA) at https://naps.ncra.tifr.res.in/goa/data/search (Section 2.3). Processed data products underlying this article will be shared on reasonable request to the authors. Access to the code-bases used throughout this work are disclosed within the paper.

REFERENCES

Akaike H., 1974, IEEE Trans. Autom. Control, 19, 716
Alexander D. M., Hickox R. C., 2012, New Astron. Rev., 56, 93
Best P. N., Kauffmann G., Heckman T. M., Brinchmann J., Charlot S., Ivezić, Ž., White S. D. M., 2005, MNRAS, 362, 25
Binney J., Alouani Bibi F., Omma H., 2007, MNRAS, 377, 142
Brienza M. et al., 2016, A&A, 585, A29
Brienza M. et al., 2017, A&A, 606, A98
Briggs D. S., 1995, in American Astronomical Society Meeting Abstracts. p. 112.02
Churazov E., Brüggen M., Kaiser C. R., Böhringer H., Forman W., 2001, ApJ, 554, 261
Condon J. J., Cotton W. D., Greisen E. W., Yin Q. F., Perley R. A., Taylor G. B., Broderick J. J., 1998, AJ, 115, 1693
Cordey R. A., 1987, MNRAS, 227, 695
Croton D. J. et al., 2006, MNRAS, 365, 11
Duchesne S. W., Johnston-Hollitt M., 2019, Publ. Astron. Soc. Aust., 36, e016
Fabian A. C., 2012, ARA&A, 50, 455
Fabian A. C., Sanders J. S., Allen S. W., Crawford C. S., Iwasawa K., Johnstone R. M., Schmidt R. W., Taylor G. B., 2003, MNRAS, 344, L43
Fanaroff B. L., Riley J. M., 1974, MNRAS, 167, 31P
Frater R. H., Brooks J. W., Whiteoak J. B., 1992, J. Electr. Electron. Eng. Aust., 12, 103
Godfrey L. E. H., Morganti R., Brienza M., 2017, MNRAS, 471, 891
Gültekin K. et al., 2009, ApJ, 698, 198
Hardcastle M. J., 2013, MNRAS, 433, 3364
Häring N., Rix H.-W., 2004, ApJ, 604, L89
Harwood J. J., Hardcastle M. J., Croston J. H., Goodger J. L., 2013, MNRAS, 435, 3353
Harwood J. J., Hardcastle M. J., Croston J. H., 2015, MNRAS, 454, 3403
Hurley-Walker N. et al., 2017, MNRAS, 464, 1146

Hurley-Walker N. et al., 2019, Publ. Astron. Soc. Aust., 36, e048
Huynh M. T., Bell M. E., Hopkins A. M., Norris R. P., Seymour N., 2015, MNRAS, 454, 952
Huynh M. T., Seymour N., Norris R. P., Galvin T., 2020, MNRAS, 491, 3395
Jaffe W. J., Perola G. C., 1973, A&A, 26, 423
Jarvis M. et al., 2016, in MeerKAT Science: On the Pathway to the SKA. p. 6, preprint (arXiv:1709.01901)
Johnston S. et al., 2007, Publ. Astron. Soc. Aust., 24, 174
Jonas J., MeerKAT Team, 2016, in Proceedings of MeerKAT Science: On the Pathway to the SKA. p. 1
Jurlin N. et al., 2020, A&A, 638, A34
Jurlin N., Brienza M., Morganti R., Wadadekar Y., Ishwara-Chandra C. H., Maddox N., Mahatma V., 2021, A&A, 653, A110
Kaiser C. R., Alexander P., 1997, MNRAS, 286, 215
Kaiser C. R., Dennett-Thorpe J., Alexander P., 1997, MNRAS, 292, 723
Kale R., Ishwara-Chandra C. H., 2021, Exp. Astron., 51, 95
Kapinska A. D., Hardcastle M., Jackson C., An T., Baan W., Jarvis M., 2015, Proc. Sci., Advancing Astrophysics with the Square Kilometre Array. SISSA, Trieste, PoS#173
Kardashev N. S., 1962, SvA, 6, 317
Komatsu E. et al., 2011, ApJS, 192, 18
Komissarov S. S., Gubanov A. G., 1994, A&A, 285, 27
Lacy M. et al., 2020, PASP, 132, 035001
Longair M. S., 2011, High Energy Astrophysics. Cambridge University Press, Cambridge
Magorrian J. et al., 1998, AJ, 115, 2285
Mahatma V. H. et al., 2018, MNRAS, 475, 4557
Mahatma V. H., Hardcastle M. J., Croston J. H., Harwood J., Ineson J., Moldon J., 2020, MNRAS, 491, 5015
McMullin J. P., Waters B., Schiebel D., Young W., Golap K., 2007, in Shaw R. A., Hill F., Bell D. J., eds, ASP Conf. Ser. Vol. 376, Astronomical Data Analysis Software and Systems XVI. Astron. Soc. Pac., San Francisco, p. 127
McNamara B. R., Nulsen P. E. J., 2007, ARA&A, 45, 117
Miley G., 1980, ARA&A, 18, 165
Morganti R., 2017, Nat. Astron., 1, 596
Murgia M. et al., 2011, A&A, 526, A148
Nagai H., Inoue M., Asada K., Kameno S., Doi A., 2006, ApJ, 648, 148
Norris R. P., 2011, J. Astrophys. Astron., 32, 599
Offringa A. R., Smirnov O., 2017, MNRAS, 471, 301
Offringa A. R., van de Gronde J. J., Roerdink J. B. T. M., 2012, A&A, 539, A95
Offringa A. R. et al., 2014, Astrophysics Source Code Library, record ascl:1408.023.
Oosterloo T., Verheijen M., van Cappellen W., 2010, in van Leeuwen J., ed., Proceedings of science, ISKAF2010 Science Meeting. p. 43, Available at: http://pos.sissa.it/cgi-bin/reader/conf.cgi?confid=112
Pacholczyk A. G., 1970, in Series of Books in Astronomy and Astrophysics. Freeman & Co., San Francisco
Parma P., Murgia M., de Ruiter H. R., Fanti R., Mack K. H., Govoni F., 2007, A&A, 470, 875
Quici B. et al., 2021, Publ. Astron. Soc. Aust., 38, e008
Reynolds J. E., 1994, ATNF Internal Memo AT/39.3/040, A Revised Flux Scale for the AT Compact Array. Australia Telescope National Facility
Rybicki G. B., Lightman A. P., 1979, Radiative Processes in Astrophysics. A Wiley-Interscience Publication, New York
Sault R. J., Teuben P. J., Wright M. C. H., 1995, in Shaw R. A., Payne H. E., Hayes J. J. E., eds, ASP Conf. Ser. Vol. 77, Astronomical Data Analysis Software and Systems IV. Astron. Soc. Pac., San Francisco, p. 433,
Schoenmakers A. P., de Bruyn A. G., Röttgering H. J. A., van der Laan H., Kaiser C. R., 2000, MNRAS, 315, 371
Shabala S. S., Jurlin N., Morganti R., Brienza M., Hardcastle M. J., Godfrey L. E. H., Krause M. G. H., Turner R. J., 2020, MNRAS, 496, 1706
Shimwell T. W. et al., 2019, A&A, 622, A1
Shimwell T. W. et al., 2022, A&A, 659, A1
Shulevski A., Morganti R., Oosterloo T., Struve C., 2012, A&A, 545, A91
Shulevski A. et al., 2017, A&A, 600, A65
Tadhunter C., 2008, Mem. Soc. Astron. Ital., 79, 1205

Tribble P. C., 1991, MNRAS, 253, 147
Turner R. J., 2018, MNRAS, 476, 2522
Turner R. J., Shabala S. S., 2015, ApJ, 806, 59
Turner R. J., Shabala S. S., 2020, MNRAS, 493, 5181
Turner R. J., Rogers J. G., Shabala S. S., Krause M. G. H., 2018a, MNRAS, 473, 4179
Turner R. J., Shabala S. S., Krause M. G. H., 2018b, MNRAS, 474, 3361
Turner R. J., Drouart G., Seymour N., Shabala S. S., 2020, MNRAS, 499, 3660
van Haarlem M. P. et al., 2013, A&A, 556, A2
Vikhlinin A., Kravtsov A., Forman W., Jones C., Markevitch M., Murray S. S., Van Speybroeck L., 2006, ApJ, 640, 691

Worrall D. M., Birkinshaw M., Young A. J., Momtahan K., Fosbury R. A. E., Morganti R., Tadhunter C. N., Verdoes Kleijn G., 2012, MNRAS, 424, 1346
Yates-Jones P. M., Shabala S. S., Krause M. G. H., 2021, MNRAS, 508, 5239
Yates-Jones P. M., Turner R. J., Shabala S. S., Krause M. G. H., 2022, MNRAS, 511, 5225

APPENDIX A:

Table A1. Summary of the integrated radio spectrum compiled for J2253-34.

Telescope	Type	Frequency (MHz)	Bandwidth (MHz)	Integrated flux density (mJy)
MWA Phase I	Survey (GLEAM)	119.04 154.88	30.72	238 ± 35 194 ± 35
uGMRT	Pointed observations	417 682	250	114.00 ± 8.88 79.8 ± 5.2
ASKAP	Survey (EMU early-science)	887	288	64.1 ± 3.2
MeerKAT	Pointed observations	911 1022 1422 1653	42 120 153 30	63.17 ± 1.89 57.44 ± 1.85 41.28 ± 1.34 35.28 ± 1.08
VLA	Survey (NVSS)	1400	50	42.4 ± 3.05
ATCA	Pointed observations	2000 2868 4782 5243 5746 6216 8284 8726 9253 9716	500	29.58 ± 1.77 19.60 ± 1.17 10.50 ± 0.42 9.38 ± 0.37 7.93 ± 0.32 6.84 ± 0.27 4.13 ± 0.19 3.84 ± 0.16 3.41 ± 0.15 3.08 ± 0.14

This paper has been typeset from a TEX/LATEX file prepared by the author.